Three-dimensional time-profile analysis of high-order harmonic generation in molecules: Nuclear interferences in H_2^+

G. Lagmago Kamta and A. D. Bandrauk
Laboratoire de Chimie Théorique, Faculté des Sciences, Université de Sherbrooke, Sherbrooke, Québec, Canada, J1K 2R1
(Received 18 November 2004; published 20 May 2005)

We describe a numerical method used previously [Phys. Rev. A **70**, 011404(R) (2004)] for solving the three-dimensional time-dependent Schrödinger equation for H_2^+ (with fixed nuclei) in interaction with an intense, arbitrary oriented laser pulse. In this approach, we use the prolate spheroidal coordinate system, and expand the time-dependent wave function in a complex basis of Laguerre polynomials and Legendre functions. Our results indicate that ionization, excitation, and harmonic generation are strongly influenced by the orientation of the molecular axis with respect to the laser polarization axis. We evaluate the contribution of each nucleus to harmonic generation, as this permits a quantitative and nonambiguous assessment of interference effects as a function of molecular orientation. A time-profile analysis, using a Gabor transform of the harmonic spectrum around certain harmonics, shows that every half-cycle high-order harmonics are emitted by *each nucleus* when the electron wave packet returns for a recollision with the molecular core, thus confirming the strong field recollision model in molecules. In general, each nucleus emits both odd and even harmonics, but even harmonics are destroyed by interferences between contributions of each nucleus. These interferences are shown to be maximum at certain harmonic orders as a function of molecular orientation. A comparison of acceleration and dipole formulations of the harmonic emission process is made in order to assess the use of high-order harmonic generation for electron wave-function imaging.

DOI: 10.1103/PhysRevA.71.053407 PACS number(s): 42.50.Hz, 33.80.−b, 42.65.Ky

I. INTRODUCTION

Current laser technology has opened up a new field of study, the nonlinear nonperturbative response of matter to intense ultrashort laser pulses [1]. In the case of atomic systems, this has led to the discovery of many new nonlinear nonperturbative optical phenomena and processes such as above threshold ionization (ATI), tunnelling ionization, and high-order harmonic generation (HOHG). The latter has become the main source for the generation of subfemtosecond, i.e., attosecond pulses [2,3].

The interaction of molecules with intense ultrashort laser pulses introduces new challenges due to the presence of nuclear motion, i.e., extra degrees of freedom, and due to additional time scales [4]. Previous studies of HOHG based on the numerical solution of the time-dependent Schrödinger equation (TDSE) for H_2^+ with both static (Born-Oppenheimer) and moving (non-Born-Oppenheimer) nuclei [5] have confirmed the applicability of the quasistatic atomic model of recollision of the ionized electron with the parent ion, or with neighboring ions [6,7] as the main mechanism for HOHG. This semiclassical recollision mechanism predicts a maximum harmonic order N_m, giving rise to the cutoff law [8,9]

$$N_m\omega_0 = I_p + 3.17U_p, \tag{1}$$

where I_p is the ionization potential, and $U_p = I/4\omega_0^2$ is the ponderomotive energy of the electron in a laser field of intensity I and frequency ω_0. The recollision of an ionized electron with neighboring ions in extended molecular systems can lead to even higher cutoffs or equivalently higher harmonic order N_m [7].

The semiclassical recollision model predicts furthermore that under the influence of the laser field, the ionized electron returns to the parent ion near the zero of the electric field, assuming that the electron ionizes with zero initial velocity via tunnelling. The recollision model has now been confirmed experimentally for H_2^+ [10] and D_2^+ [11]. These experiments confirm that ultrashort time scales are characteristic of electron recollision and depend on the laser frequency only. This suggests that Born-Oppenheimer (i.e., fixed nuclei) simulations of molecular HOHG should be useful in exploring the effect of laser-induced electron diffraction (LIED) [12], and the concomitant interferences arising from rescattering of the recolliding electron wave packet with different nuclei observed recently in a molecular simulation of ATI [13].

Molecular HOHG offers another variation upon the atomic case, the orientation dependence of this nonlinear response to short intense pulses [14], whose orientation depends on laser intensities [15]. Experiments have also shown that HOHG in molecules is enhanced when molecules are prealigned, and that there is a high sensitivity of the efficiency of the HOHG spectrum with the relative orientation of the molecule and the laser pulse polarization [16]. Recent H_2^+ and H_2 reduced model calculations [17,18] confirm the importance of interference contributions to HOHG from various regions within a molecule as in previous calculations of LIED [12] and molecular ATI [13].

In this paper, we present an exact numerical solution of the three-dimensional (3D) Born-Oppenheimer (static nuclei) TDSE for the interaction of H_2^+ with a laser pulse having an arbitrary oriented linear polarization. We investigate the influence of molecular orientation on ionization and harmonic generation. The contribution of each nucleus to the harmonic

spectrum is evaluated separately, so that interferences of the two contributions are assessed unambiguously (preliminary results have been reported in an earlier communication [19]). A time-frequency analysis of the generation of harmonics is performed using a Gabor transform technique [20,21], so that the magnitude of relevant interferences and their enhancement or suppression are identified in time. Furthermore, we examine the usefulness of a Frank-Condon model of HOHG intensities and their orientation dependence, as a direct transition from a continuum electron wave function to the ground-state electron wave function. This usually occurs in continuum molecular Raman transition [22] or harmonic interference ionization spectra [23]. Dipole and acceleration formulations [24] of the photoemission process are compared in order to establish a valid theoretical description of the interference effects. The sensitivity of HOHG intensities to the molecular orientation have recently been proposed as a new tool for tomographic reconstruction of molecular electronic orbitals [25]. The present results provide guidelines for such an inversion procedure based on HOHG spectra, as we provide a rigorous derivation of analytical formulas for the interference in the harmonic spectra of two-center molecules.

This paper is organized as follows. In Sec. II, we describe the complex basis in which the time-dependent wave function is expanded. The solution of the TDSE is presented in Sec. III, where we also discuss the advantages of the method used. Results for ionization and excitation are given in Sec. IV. The contribution of each nucleus to the harmonic spectrum of H_2^+ is analyzed in Sec. V. Section VI is devoted to a study of interference effects in the harmonic generation of H_2^+. We compare the acceleration and dipole formulations of the harmonic photoemission in Sec. VII. After a conclusion in Sec. VIII, we present in two appendices the evaluation of matrix elements involved in the solution of the TDSE. Unless stated otherwise, atomic units (a.u.) are used throughout this paper.

II. THE WAVE-FUNCTION EXPANSION

In the Born-Oppenheimer approximation (fixed nuclei), the electronic Hamiltonian for a system consisting of two nuclei having identical charge Z, and one active electron is

$$H = -\frac{1}{2}\nabla^2 + V(r) + \frac{Z^2}{R}, \tag{2}$$

where R is the internuclear distance, and

$$V(r) = V_1(r) + V_2(r) = -\frac{Z}{r_1} - \frac{Z}{r_2} \tag{3}$$

is the Coulomb potential experienced by the electron due to both nuclei. $\mathbf{r}_1 = \mathbf{r} + \mathbf{R}/2$ and $\mathbf{r}_2 = \mathbf{r} - \mathbf{R}/2$ are the position vectors of the electron relative to the nucleus 1 and relative to the nucleus 2, respectively. $\mathbf{r}$ is the position vector of the electron relative to the geometric center of the molecule.

The interaction of the above system with a laser field is described by the TDSE

$$i\frac{\partial}{\partial t}\Psi(\mathbf{r},t) = [H + D(t)]\Psi(\mathbf{r},t), \tag{4}$$

where the Hamiltonian $D(t)$ for the interaction of the electron with the laser field is $D_L(t) = \mathbf{E}(t)\cdot\mathbf{r}$ in the length gauge, and is $D_V(t) = -i\mathbf{A}(t)\cdot\nabla$ in the velocity gauge. The vector potential $\mathbf{A}(t)$ of the laser field is $\mathbf{A}(t) = A_0 f(t)\sin(\omega_0 t)\mathbf{e}$, where A_0 is the maximum amplitude, $f(t)$ is the pulse envelope, ω_0 is the laser frequency, and $\mathbf{e}$ is the unit vector along the laser polarization axis. The electric field of the laser pulse is derived from $\mathbf{A}(t)$ as $\mathbf{E}(t) = -(\partial/\partial t)\mathbf{A}(t)$.

For convenience, we make the following choices, which do not impose any physical restriction on the system: (i) The molecular axis is aligned along the z axis, i.e., $\mathbf{R} = R\mathbf{e}_z$, where $\mathbf{e}_j$ denotes the unit vector along the j axis. (ii) The laser polarization is chosen in the yz plane, so that $\mathbf{e} = \sin(\chi)\mathbf{e}_y + \cos(\chi)\mathbf{e}_z$. Therefore, $D_L(t) = E(t)[(\sin\chi)y + (\cos\chi)z]$ and $D_V(t) = -iA(t)[(\sin\chi)(\partial/\partial y) + (\cos\chi)(\partial/\partial z)]$. Since the molecule is aligned along the z axis, then χ is the angle between the z axis and the laser polarization direction.

The electronic angular momentum operator L^2 and its projection L_z along the z axis satisfy the relations $[L^2, H] \neq 0$ and $[L_z, H] = 0$. This means that in the absence of external field, a two-center molecule does not have spherical symmetry, but does have axial symmetry. Consequently, the projection m of the electronic angular momentum along the internuclear axis L_z is conserved. In the presence of a laser field linearly polarized along the molecular axis (i.e., $\chi = 0$), the axial symmetry is preserved. In this case, the solution of the resulting TDSE is in essence a two-dimensional (2D) problem due to this axial symmetry. However, for an arbitrary oriented laser polarization, as considered in this work, the existence of a component of the electric field perpendicular to the molecular axis breaks the axial symmetry, so that the angular momentum projection m is no longer conserved. Solving the TDSE for this case is by all means a fully 3D problem.

Prolate spheroidal coordinates are well established as the most adequate coordinate system for investigating the molecular structure of two-center molecules [26]. These coordinates (ξ, η, ϕ) are defined by

$$\xi = (r_1 + r_2)/R, \quad \eta = (r_1 - r_2)/R, \tag{5}$$

where ϕ is the azimuthal angle, $1 \leqslant \xi \leqslant +\infty$, $-1 \leqslant \eta \leqslant +1$, and $0 \leqslant \phi \leqslant 2\pi$. Expressions in spheroidal coordinates of the Hamiltonian H, the coordinates (x, y, z), and their derivatives $(\partial/\partial x, \partial/\partial y, \partial/\partial z)$ can be found in Ref. [27].

For a two-center molecule, the stationary Schrödinger equation $H\Psi = E\Psi$ is separable in spheroidal coordinates. Due to this separability, it is suitable to expand the time-dependent wave function in a discrete basis as follows:

$$\Psi(\xi,\eta,\phi,t) = \sum_{m,\mu,\nu} a_{m\mu\nu}(t) U_\nu^m(\xi) V_\mu^m(\eta) \frac{e^{im\phi}}{\sqrt{2\pi}}, \tag{6}$$

where $a_{m\mu\nu}(t)$ are time-dependent coefficients. The basis functions $U_\nu^m(\xi)$ and $V_\mu^m(\eta)$ are given by

$$U_\nu^m(\xi) = N_\nu^m e^{-\alpha(\xi-1)}(\xi^2-1)^{|m|/2} L_{\nu-|m|}^{2|m|}[2\alpha(\xi-1)] \quad (7)$$

and

$$V_\mu^m(\eta) = M_\mu^m P_\mu^m(\eta), \quad (8)$$

where $\alpha=\beta R$ and β is a real or complex parameter to be discussed later. $L_p^q(x)$ denotes the Laguerre polynomials, and $P_p^q(x)$ is the associated Legendre function (or spherical function) of the first kind [28]. m is the electron's angular momentum projection onto the z axis. It takes the values $m=0,\pm1,\pm2,\ldots,\pm m_{\max}$. The two other indices take the values $\mu=|m|,|m|+1,\ldots,|m|+\mu_{\max}$ and $\nu=|m|,|m|+1,\ldots,|m|+\nu_{\max}$. $m_{\max}$, $\mu_{\max}$, and $\nu_{\max}$ are cutoff parameters used to control the basis size.

We use the following normalization conditions for the basis functions:

$$\int_1^{+\infty} U_\nu^m(\xi)\left(\frac{\xi-1}{\xi+1}\right)^{|m|} U_\nu^m(\xi)d\xi = 1 \quad (9)$$

and

$$\int_{-1}^{+1} V_\mu^m(\eta) V_\mu^m(\eta)d\eta = 1, \quad (10)$$

which lead to

$$N_\nu^m = \sqrt{(2\alpha)^{2|m|+1}\frac{(\nu-|m|)!}{(\nu+|m|)!}} \quad (11)$$

and

$$M_\mu^m = \sqrt{\left(\mu+\frac{1}{2}\right)\frac{(\mu-m)!}{(\mu+m)!}}. \quad (12)$$

The normalization conditions (9) and (10) are interesting because they lead to analytical expressions for N_ν^m and M_μ^m. In addition, the resulting normalization constants N_ν^m and M_μ^m are crucial in preventing the basis functions $U_\nu^m(\xi)$ and $V_\mu^m(\eta)$ from taking very large values with increasing m. Such large values lead to numerical instabilities. Finally, the basis function $V_\mu^m(\eta)$ inherits interesting properties such as $V_\mu^{-m}(\eta)=(-1)^m V_\mu^m(\eta)$ and $V_\mu^m(-\eta)=(-1)^{(\mu+m)}V_\mu^m(\eta)$.

Since $P_\mu^m(\eta)=(-1)^m(1-\eta^2)^{m/2}(d^m/d\eta^m)P_\mu(\eta)$ [28], it appears that the basis functions $U_\nu^m(\xi)$ and $V_\mu^m(\eta)$ depend on the factors $(\xi^2-1)^{|m|/2}$ and $(1-\eta)^{|m|/2}$, respectively. This feature has been shown to removes singularities in the Hamiltonian H [26]. In addition, a semianalytic solution of the stationary Schrödinger equation for H_2^+ is greatly simplified by writing the wave function of H_2^+ in terms of Laguerre polynomials and associated Legendre functions [26]. These functions permit to recover the well-known hydrogenlike wave functions in the united-atom limit (i.e., $R\to0$). Basis expansions similar to (6) have been used successfully for molecular structure [29] and multiphoton ionization rate calculations for H_2^+ [27], as well as for time-dependent calculations in H_2^+ with laser pulses linearly polarized along the internuclear axis [30]. It is worth mentioning that the basis expansion (6) mimics the Sturmian basis used for the spherically symmetric case of hydrogen [31].

As mentioned above, for the case of a laser field linearly polarized along the z axis, m is conserved. This means that if the initial state is the ground state of H_2^+ for which $m=0$, one can set $m=0$ in the basis expansion (6). If there is a component of the laser field perpendicular to the internuclear axis, one has to include higher m values in the expansion (6).

Throughout the time evolution of the exact solution $\Psi(\xi,\eta,\phi,t)$, the quantity $\langle\Psi(t)|\Psi(t)\rangle$, which represents the probability for finding the electron somewhere in the whole space, remains constant and equal to unity. The computation of $\langle\Psi(t)|\Psi(t)\rangle$ requires an integration over all the space. In practice, however, due to limitations in computer resources, the expansion (6) should be truncated. Therefore, the resulting approximate wave function only describes a restricted region of space, say, a sphere of some characteristic radius. As long as the system remains in this sphere over the time interval of interest, the truncated basis is adequate. But if the system breaks up during its time evolution, as it is the case when ionization occurs, one or more fragments of the system may leave this sphere. Nevertheless, if the basis functions $U_\nu^m(\xi)$ are real, the norm $\langle\Psi(t)|\Psi(t)\rangle$ computed with the truncated wave-function expansion remains constant equal to unity throughout the time evolution [32]. This means that the probability of finding the complete system inside the sphere is always unity on a real basis. Therefore, if the system breaks up with one of its fractions reaching the surface of the sphere over the time interval under interest, the fact that $\langle\Psi(t)|\Psi(t)\rangle=1$ with a real basis means that this fragment must reflect from the surface and return to the interior of the sphere.

These reflections are unphysical and must be prevented by absorbing the outgoing flux at the boundary of the sphere. This may be achieved by imposing strictly outgoing wave boundary conditions on the wave function itself. It has been shown [33] that complex scaling [34] in the solution of the TDSE analytically prevents reflection of outgoing wave packets. In prolate spheroidal coordinates, complex scaling can be implemented [35] by making the transformation $(\xi,\eta,\phi)\to(e^{i\theta}\xi,\eta,\phi)$ in the Hamiltonian, or equivalently, by making the transformation $(\xi,\eta,\phi)\to(e^{-i\theta}\xi,\eta,\phi)$ in the wave function, where θ is the complex scaling "angle." For the basis expansion (6), the complex scaling method amounts to using a complex nonlinear parameter $\beta=|\beta|e^{-i\theta}$ $(0<\theta<\pi/2)$, and the resulting basis functions $U_\nu^m(\xi)$ behave asymptotically as outgoing waves. This asymptotic outgoing behavior prevents reflections at the boundaries of the region described by the truncated wave-function expansion.

III. THE PROPAGATION OF THE TIME-DEPENDENT SCHRÖDINGER EQUATION

In order to solve the TDSE (4), we project it onto the basis expansion (6) to obtain its matrix representation

$$i\frac{\partial}{\partial t}\mathbf{S}\boldsymbol{\Psi} = [\mathbf{H} + g(t)(\sin\chi\mathbf{D}_y + \cos\chi\mathbf{D}_z)]\boldsymbol{\Psi}, \quad (13)$$

where $\boldsymbol{\Psi}$ represents the vector representation of the wave function, and $\mathbf{S}$ is the overlap matrix. $\mathbf{H}$, $\mathbf{D}_y$, and $\mathbf{D}_z$ denote,

respectively, the matrix elements of the electronic Hamiltonian, and those of the y and z components of the dipole operator (length or velocity gauges). $g(t)$ is a scalar function that equals $E(t)$ in the length gauge, and equals $-iA(t)$ in the velocity gauge.

Details on the evaluation of the matrix elements of $\mathbf{S}$, $\mathbf{H}$, $\mathbf{D}_y$, and $\mathbf{D}_z$ are given in Appendices A and B. Thanks to the separability of spheroidal coordinates, all these matrix elements can be expressed as products of one-dimensional integrals, many of which are obtained in closed analytical forms. Those integrals that could not be obtained analytically are evaluated numerically using Gauss-Laguerre and Gauss-Legendre quadratures, which are very stable and accurate.

As shown in these appendices, the basis expansion (6) yields interesting selection rules; $\mathbf{S}$, $\mathbf{H}$, and $\mathbf{D}_z$ matrix elements are subjected to the selection rule $m'=m$, whereas $\mathbf{D}_y$ matrix elements are subjected to $m'=m\pm1$. In other words, the z component of the dipole couples only states that have identical angular momentum projections, whereas the y component of the dipole couples states whose angular momentum projections differ by unity. Due to these selection rules, all matrices involved in Eq. (13) are very sparse: $\mathbf{H}$, $\mathbf{S}$, and $\mathbf{D}_z$ are bloc diagonal, whereas $\mathbf{D}_y$ is bloc tridiagonal. Here, each bloc corresponds to a given (m',m) pair, and the nonzero blocs are those for which the selection rules $m'=m$ and $m'=m+1$ hold.

In order to obtain the initial state for time propagation of the TDSE (13), we solve the the stationary Schrödinger equation, which is equivalent to solving the eigenvalue problem

$$\mathbf{H}\boldsymbol{\Psi} = E\mathbf{S}\boldsymbol{\Psi}, \tag{14}$$

where E denotes the requested eigenvalues. Note that, due to complex scaling, $\mathbf{H}$ and $\mathbf{S}$ are complex symmetric, so that the eigenvalues E are complex. However, bound state energies are independent of the complex scaling angle θ, whereas continuum states are rotated downward in the lower half of the complex plane, making an angle 2θ with the real axis [34]. In other words, bound states are unchanged by complex rotation.

Solving the generalized eigenvalue problem (14) yields not only the initial state, but also a set of bound states and discretized continuum states. The number and the accuracy of such bound and continuum states depend on the number of terms in the basis expansion. The accuracy of these states also depends on the nonlinear parameter β used [36]. Therefore, the solution of the eigenvalue equation (14) provides an insight into the accuracy of the basis expansion (6), by comparison of the energies obtained with reference data. Table I shows energies of the first ten energies of H_2^+ (with the nuclei repulsion $1/R$ excluded) for various angular momentum projections m up to $|m|=12$. Energies given in this table are accurate up to all digits shown. This high accuracy achieved for eigenstate energies suggests that the basis expansion (6) is very suitable for describing H_2^+.

Another insight into the accuracy of the wave-function expansion (6) can be gained through dipole matrix elements. Figure 1 shows the dipole matrix elements obtained for the $1s\sigma_g \rightarrow 2s\sigma_u$ transition for various internuclear distances. Our results in Fig. 1 are plotted together with dipole matrix element formula [37] obtained using a linear combination of atomic orbitals (LCAO). As expected, as small internuclear distances where LCAO wave functions are known to be quite inaccurate, there are substantial differences between the approximate LCAO results and our exact results. However, with increasing internuclear distance the LCAO approximation becomes increasingly valid, and one can see that LCAO results get closer to our exact results.

Equation (13) is a system of first-order partial differential equations (PDEs), which can be solved using standard numerical procedures. However, for reasons described below, we project it into the basis of electronic eigenstates (i.e., the so-called eigenstate basis [38,39]) where it becomes

$$i\frac{\partial}{\partial t}\boldsymbol{\Phi} = [\mathbf{h} + g(t)(\sin\chi\mathbf{W}_y + \cos\chi\mathbf{W}_z)]\boldsymbol{\Phi}, \tag{15}$$

where $\boldsymbol{\Phi}(t)=\mathbf{P}^t\boldsymbol{\Psi}(t)$, and where the exponent t denote the transposed of the corresponding matrix. $\mathbf{h}$ is the diagonal matrix of eigenvalues of $\mathbf{H}$ (electronic energies). $\mathbf{P}$ is the orthogonal matrix of eigenvectors of $\mathbf{H}$ (electronic wave functions), i.e., $\mathbf{h}=\mathbf{P}^t\mathbf{H}\mathbf{P}$. $\mathbf{W}_j=\mathbf{P}^t\mathbf{D}_j\mathbf{P}$ is the matrix of dipole couplings between all electronic eigenstates $(j=y,z)$. The projected wave function $\boldsymbol{\Phi}(t)$ in the eigenstate basis represents a linear superposition of all electronic eigenstates resulting from solving the eigenvalue equation (14), i.e.,

$$\boldsymbol{\Phi}(t) = \sum_{m,n} C_{m,n}(t)\boldsymbol{\Phi}_{m,n}, \tag{16}$$

where $\boldsymbol{\Phi}_{m,n}$ is the electronic eigenstate of energy E_n and angular momentum projection m, and $C_{m,n}(t)$ is its probability amplitude. n labels both bound states and the discretized continuum. Note that $\boldsymbol{\Psi}(t)$ can be easily deduced from $\boldsymbol{\Phi}(t)$ by the matrix vector product $\boldsymbol{\Psi}(t)=\mathbf{P}\boldsymbol{\Phi}(t)$. This last transformation permits us to move back and forth between the eigenstate representation $\boldsymbol{\Phi}$ of the wave function and its coordinate representation $\boldsymbol{\Psi}$.

Besides the selection rules $m'=m$ and $m=m\pm1$ mentioned earlier for the matrix elements of the dipole operator, the fact that we are dealing with an homonuclear molecule gives rise to another selection rule: the dipole operator couples only eigenstates having different parity. In other words, the dipole couples only gerade states with ungerade states, so that in the dipole matrix $\mathbf{W}_j$ in the eigenstate representation, all elements coupling only gerade states vanish, as well as those coupling only ungerade states. Therefore, one can arrange the components $C_{m,n}(t)$ of $\boldsymbol{\Phi}(t)$ in increasing m values such that for each m, all components corresponding to gerade (g) states are arranged sequentially, followed by all those corresponding to ungerade states. Consequently, for each nonzero (m',m) bloc of the matrix $\mathbf{D}_j$, the corresponding bloc in the matrix $\mathbf{W}_j$ is split into four nearly equal sub-blocs, among which two are zero. The increased sparsity in $\mathbf{W}_j$, combined with the fact that $\mathbf{h}$ is diagonal indicates clearly that the TDSE (15) in the eigenstate representation is much sparser that its analog (13). As discussed below, this is an interesting computational advantage for the eigenstate representation. Another advantage of this representation is that $|C_{m,n}(t)|^2$ is

TABLE I. Absolute values of energies (nuclei repulsion $1/R$ excluded) of the first ten bound states of H_2^+ for various values of the electron's angular momentum projection m up to $|m|=11$. The equilibrium internuclear distance $R=2$ a.u. is used. The superscript g and u specifies the symmetry gerade or ungerade of the eigenstate. Energies are given in atomic units.

$m=0$	$m=\pm1$	$m=\pm2$	$m=\pm3$
1.1026342145^g	0.42877181990^u	0.21273268181^g	0.12312550080^u
0.66753439220^u	0.22669962664^g	0.12496254294^u	0.07986919551^g
0.36086487534^g	0.20086482991^u	0.12101946275^g	0.07904328586^u
0.25541316509^u	0.12671013067^g	0.08014600689^g	0.05556674393^u
0.23577762883^g	0.12619892053^u	0.07997419943^u	0.05547938897^g
0.17768104513^g	0.11591529004^u	0.07796553506^g	0.05500270852^u
0.13731292428^u	0.08083489934^g	0.05563963169^g	0.04083181867^g
0.13079187763^g	0.08061122322^u	0.05562458478^u	0.04082330650^u
0.12664387015^u	0.08031607574^g	0.05553856586^u	0.04076818295^g
0.10544230117^g	0.07532056626^u	0.05437870191^g	0.04046842876^u
$m=\pm4$	$m=\pm5$	$m=\pm6$	$m=\pm7$
0.07949446111^g	0.05538472492^u	0.04074836411^g	0.03121946244^u
0.05548654454^u	0.04078221208^g	0.03123251806^u	0.02468193050^g
0.05526340422^g	0.04070881742^u	0.03120448535^g	0.02466991435^u
0.04081006084^g	0.03124359573^u	0.02468682771^g	0.01999701269^u
0.04077281964^u	0.03122713993^g	0.02467907910^u	0.01999312727^g
0.04063248607^g	0.03117800508^u	0.02465939833^g	0.01998436945^u
0.03125268028^u	0.02469097684^g	0.01999905547^u	0.01652804417^g
0.03124579033^g	0.02468685749^u	0.01999669677^g	0.01652668104^u
0.03122083254^u	0.02467529964^g	0.01999104822^u	0.01652376198^g
0.03112689445^g	0.02464080593^u	0.01997670464^g	0.01651718314^u
$m=\pm8$	$m=\pm9$	$m=\pm10$	$m=\pm11$
0.02467628832^g	0.01999199041^u	0.016524404477^g	0.01388620671^u
0.01999465741^u	0.01652575980^g	0.013886937819^u	0.01183307502^g
0.01998901532^g	0.01652290828^u	0.013885406600^g	0.01183220998^u
0.01652697311^g	0.01388759952^u	0.011833453668^g	0.01020348925^u
0.01652491168^u	0.01388645043^g	0.011832784970^u	0.01020308522^g
0.01652067327^g	0.01388425422^u	0.011831580695^g	0.01020239264^u
0.01388819175^u	0.01183379632^g	0.010203695398^u	0.00888860431^g
0.01388738491^g	0.01183330539^u	0.010203388373^g	0.00888840726^u
0.01388579714^u	0.01183240162^g	0.010202852988^u	0.00888807877^g
0.01388253282^g	0.01183067436^u	0.010201888822^g	0.00888751570^u

the projection of the time-dependent wave function onto the electronic state of energy E_n and angular momentum projection m. This means that the evolution of each electronic state can be traced throughout the laser excitation.

Our numerical experiments, as well as previous similar work on the H atom [31], indicate that the system of nonlinear PDE (13) is stiff [40] due to different scales in the matrix elements of $\mathbf{S}$, $\mathbf{H}$, $\mathbf{D}_y$, and $\mathbf{D}_z$. Working in the eigenstate representation (15) attenuates this stiffness. However, with increasing laser intensity and basis size the stiffness becomes increasingly serious even in the eigenstate representation. When an explicit method such as Runge-Kutta [40] is used to propagate the TDSE, the stiffness translates into the requirement of a smaller and smaller time step to maintain the stability of the integration, even though accuracy requirements allow for a much larger stepsize. The simplest cure for this problem is to use an implicit method [40] that is stable in principle for all stepsizes. The penalty is that implicit methods require matrix inversions at each step. On the other hand, explicit methods require only matrix-vector products necessary to compute the time derivative, i.e., right-hand side of Eqs. (13) or (15). With the large basis size involved in this work, the computation time and memory costs of inverting large complex matrices far outweigh the smaller stepsizes required by explicit methods. This is particularly true in this work because the matrices $\mathbf{h}$, $\mathbf{W}_y$, and $\mathbf{W}_z$ in Eq. (15) are

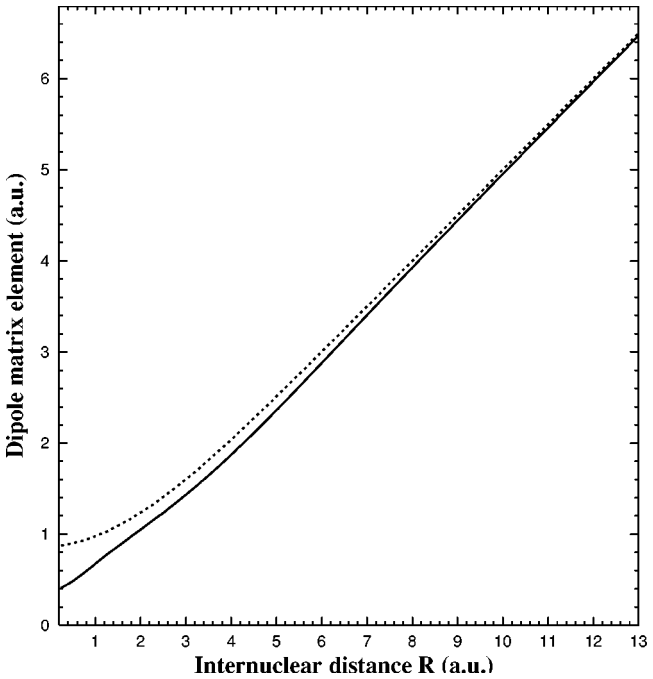

FIG. 1. Dipole matrix elements for the $1s\sigma_g \rightarrow 1s\sigma_u$ transition in H_2^+ for various internuclear distances. Results from our exact numerical approach (solid lines) are compared with those obtained using LCAO wave functions (dashed lines) [37].

very sparse. Consequently, the computation of the right-hand side of Eq. (15) is very fast, provided that one exploits this sparsity. In this perspective, the eigenstate representation (15) has an advantage over the original representation (13) because the higher sparsity of matrices in the former case leads to a faster computation of the time derivative.

In this work, we use an embedded Runge-Kutta method of order 4 with an adaptative stepsize [41] to solve the TDSE (15). We have developed an algorithm that is very fast, as it exploits the sparsity of the matrices $\mathbf{h}$ and $\mathbf{W}_j$ $(j=y,z)$ to perform matrix-vector operations. Furthermore, we use parallel computing resources to speed up the matrix-vector product by distributing the contribution of each bloc of $\mathbf{W}_j$ to parallel processors.

Results discussed throughout this paper have been obtained with the following basis parameters: $|\beta|=0.2$, $\theta=0.1$, $m_{max}=30$, $\mu_{max}=30$, and $\nu_{max}=70$, leading to about 135 000 basis functions. Results are considered converged when they remain almost unchanged with increasing basis size. We use a laser pulse of frequency $\omega_0=0.057$ a.u. (800 nm). We use a "trapezoidal" pulse envelope, i.e., the pulse is turned on linearly over three laser periods, kept at constant intensity for four laser periods, and turned off linearly over three laser periods. This corresponds to a total of ten laser periods (26 fs). The equilibrium internuclear distance $R=2$ a.u. is used.

IV. IONIZATION AND EXCITATION

The probability for finding the system in the electronic eigenstate of energy E_n and angular momentum projection m at time t_{end} (the end of laser excitation) is given by $P_{n,m}=|C_{m,n}(t_{end})|^2$. Thus, the total ionization probability at the end of the laser pulse is

$$P_{ion}=1-\sum_{m,E_n<0}|C_{m,n}(t_{end})|^2, \tag{17}$$

where the summation spans all m and all bound states, which are characterized by $E_n<0$. The ionization probability of H_2^+, obtained in the length and velocity gauges, is plotted versus the orientation angle χ in Fig. 2. For the two laser peak intensities ($I=3\times10^{14}$ W/cm^2 and $I=5\times10^{14}$ W/cm^2) shown, there is a strong dependence of the ionization on the orientation of H_2^+ relative to the laser polarization axis. The ionization probability is maximum for $\chi=0$ (parallel orientation of the molecule), and decreases with increasing χ to reach a minimum for $\chi=\pi$ (perpendicular orientation of the molecule). This pattern appears to be independent of the peak intensity of the laser, and of the gauge used for the computation.

Results in Fig. 2 show that there is a good agreement between results from the length and velocity gauges, which is another illustration of the accuracy and stability of our calculations. Our numerical simulations indicate that convergence of results is easier to achieve in the velocity gauge than in the length gauge, as the latter requires more angular momenta (i.e., a larger μ_{max} and m_{max}) in the basis expansion for convergence. This agrees with previous numerical experiments in atoms [42]. For the intensity $I=3\times10^{14}$ W/cm^2 [see Fig. 2(a)], results from the two gauges agree very well, with the largest percentage difference of 6.5% occurring at the parallel orientation. At the higher intensity $I=5\times10^{14}$ W/cm^2 [see Fig. 2(b)], both gauges still agree well, but there are more discrepancies in the vicinity of the perpendicular orientation. In fact, for this orientation, the dipole operator exclusively couples electronic eigenstates having different angular momentum projections m. This means that with increasing laser intensity, higher m values need to be included in the basis expansion, making it harder to achieve convergence in the length gauge.

Provided that the length gauge is used [43], $|C_{m,n}(t)|^2$ is the probability of finding the system at any time t in the electronic eigenstate of angular momentum m and energy E_n. Therefore, $P_{ion}(t)=1-\Sigma_{m,E_n<0}|C_{m,n}(t)|^2$ is the ionization probability of the system at an arbitrary time t, when the length gauge is used [43]. The time evolution of the ionization probability, for the orientation angle $\chi=60°$ and laser peak intensity $I=5\times10^{14}$ W/cm^2, is plotted in Fig. 3, together with the electric field (divided by 20) of the laser pulse. Figure 3 indicates that for every half-cycle, the ionization probability increases sharply when the electric field increases towards an extremum, and then decreases slightly when the electric field decreases towards zero.

The total excitation probability, i.e., the probability for finding the system in excited states, is given by $\Sigma_{m,E_n<0}|C_{m,n}(t)|^2-|C_{0,0}(t)|^2$, where $|C_{0,0}(t)|^2$ is the probability for finding the system in the ground state at time t. The time evolution of the excitation probability (also calculated in the length gauge) is shown in Fig. 4, with the electric field

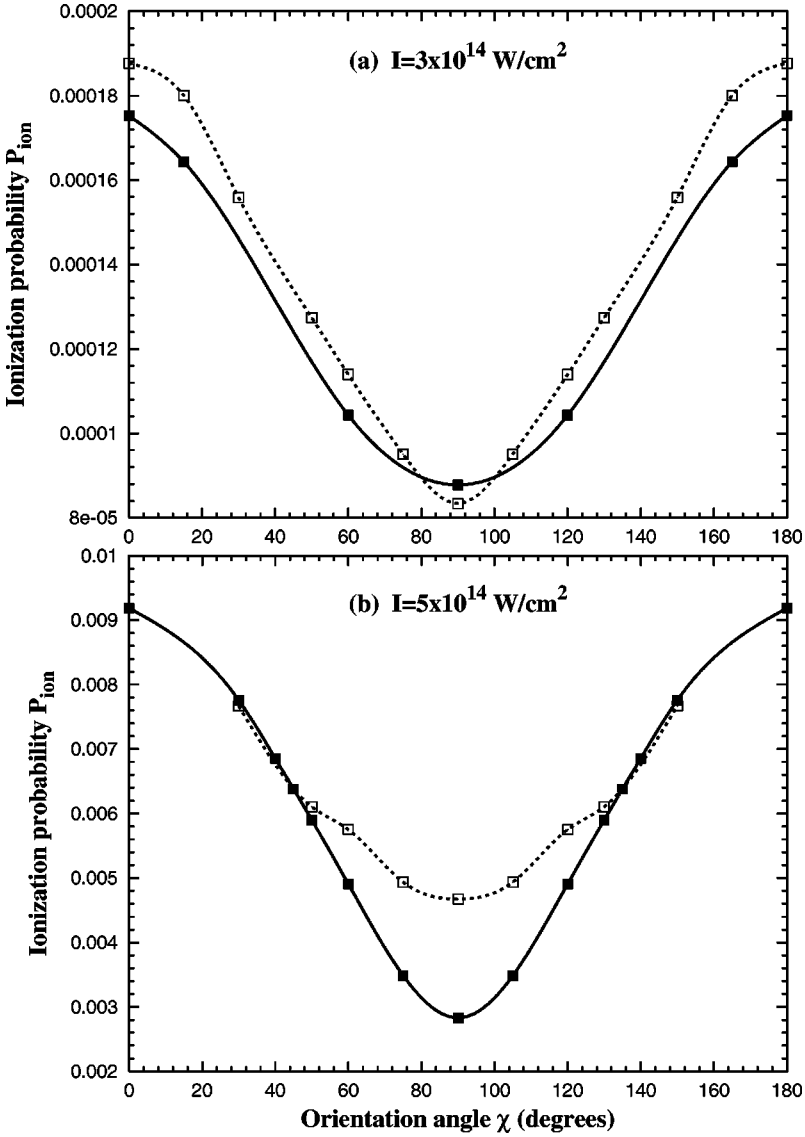

FIG. 2. Ionization probability of H_2^+ vs the orientation angle χ of molecule. Results are shown for two peak intensities of the laser: (a) $I=3\times10^{14}$ W/cm^2; (b) $I=5\times10^{14}$ W/cm^2. The empty squares (length gauge) and the filled squares (velocity gauge) are the calculated data, while the lines are drawn to guide the eye. The equilibrium internuclear distance $R=2$ a.u. is used. Laser frequency used: $\omega_0=0.057$ a.u. The pulse consists of a linear turnon over three laser periods, followed by four laser periods at constant peak intensity, and linear turnoff over three laser periods.

(divided by 10) superimposed. It appears that the excitation probability is clearly driven by the electric field, as it increases sharply with the magnitude of the electric field, and then decreases almost to zero when the electric field tends to zero. The electronic response follows the field so that one is in the adiabatic regime [44].

V. NUCLEAR CONTRIBUTIONS TO HARMONIC GENERATION

The harmonic spectrum $S(\omega)$ radiated by a system is proportional to the absolute square of the Fourier transform $A_{\mathbf{e}}(\omega)$ of the dipole acceleration [24],

$$A_{\mathbf{e}}(\omega) = \int e^{i\omega t}\langle\Psi(t)|\mathbf{e}\cdot[\nabla V(r)+\mathbf{E}(t)]|\Psi(t)\rangle dt. \quad (18)$$

$\langle\Psi(t)|\nabla V(r)+\mathbf{E}(t)|\Psi(t)\rangle$ is the dipole acceleration obtained via Ehrenfest's theorem [24]. The second term in Eq. (18) is the Fourier transform of the electric field, whose contribution to the harmonic spectrum is essentially limited to the fundamental harmonic. It follows that the high-order harmonic spectrum from the system is almost completely determined by $|G(\omega)|^2$, where

$$G(\omega) = \int e^{i\omega t}\langle\Psi(t)|\mathbf{e}\cdot\nabla V(r)|\Psi(t)\rangle dt. \quad (19)$$

Since $V(r)=V_1(r)+V_2(r)$, then we may separate the nuclear contributions

$$G(\omega) = G_1(\omega) + G_2(\omega), \quad (20)$$

where

$$G_j(\omega) = \int e^{i\omega t}\langle\Psi(t)|\mathbf{e}\cdot\nabla V_j(r)|\Psi(t)\rangle dt, \quad (21)$$

with $j=1,2$. Equations (19) and (21) indicate that $G_j(\omega)$ is the analog of $G(\omega)$ for the nucleus j. This suggests the interpretation of $|G_j(\omega)|^2$ as the harmonic spectrum originating from the nucleus j, in the presence of the other nucleus.

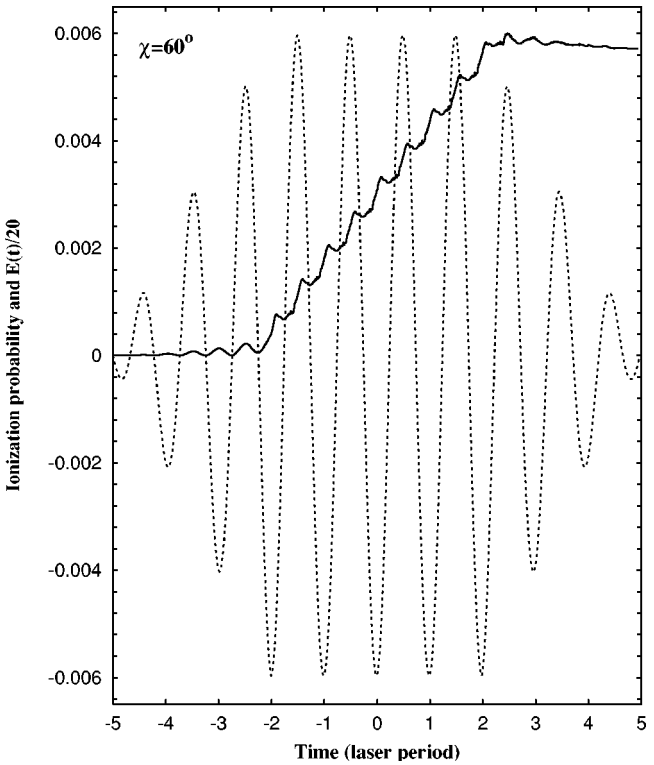

FIG. 3. Time evolution of the ionization probability of H_2^+ (solid lines) and of the electric field of the laser pulse (dashed lines). This ionization probability is computed in the length gauge, with the molecular orientation angle $\chi=60°$ and a laser peak intensity $I=5\times10^{14}$ W/cm^2. For a better comparison of the two plots, the electric field is divided by 20, i.e., $E(t)/20$ is actually plotted. Time is given in units of the laser period. The internuclear distance and laser pulse duration used are the same as in Fig. 2.

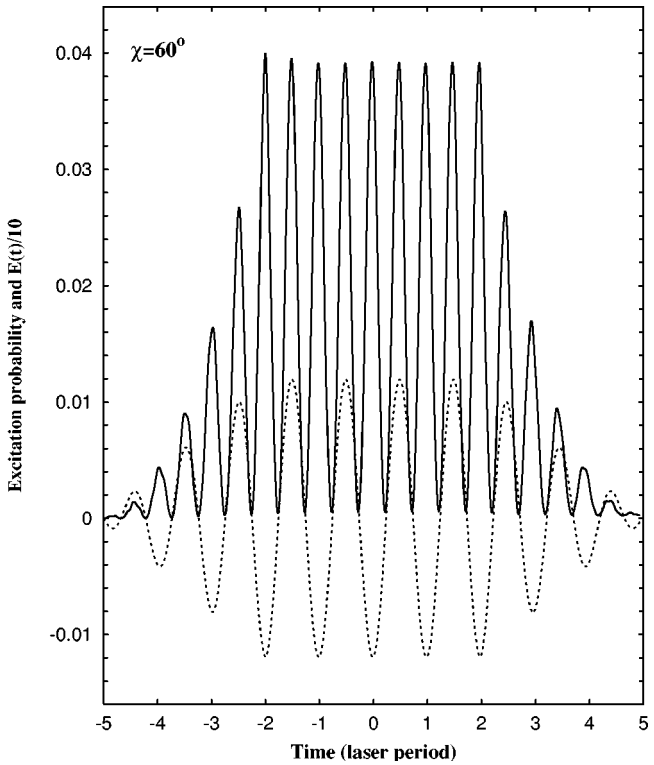

FIG. 4. Time evolution of the total excitation probability of H_2^+ (solid lines) and of the electric field of the laser pulse (dashed lines). This excitation probability is computed using the length gauge, a molecular orientation angle $\chi=60°$, and a laser peak intensity $I=5\times10^{14}$ W/cm^2. For a better comparison of the two plots, the electric field is divided by 10, i.e., $E(t)/10$ is actually plotted. Time is given in units of the laser period. The internuclear distance and laser pulse duration are the same as in Fig. 2.

Figure 5 shows the harmonic spectra originating from the nucleus 1 (i.e., $|G_1(\omega)|^2$) and from the nucleus 2 (i.e., $|G_2(\omega)|^2$) of H_2^+, for various orientations χ of the molecule with respect to the laser polarization. In both cases, and for all orientations, features of these spectra strongly resembles those of harmonic spectra from atoms: a sharp decrease of the first few harmonics, followed by a "plateau," and ending with a cutoff that determines the highest harmonic order achievable. The cutoff is independent of the molecular orientation and is located approximately at the 85th harmonic, which is in agreement with the energy cutoff formula given by Eq. (1). However, except for the orientation $\chi=90°$, there is a feature in Fig. 5 that does not exist in the harmonic spectra from atoms. This feature is the presence of both *odd* and *even* harmonics. Even harmonics do not appear in the spectra of atoms due to the inversion symmetry that exists in these systems as a result of their spherical symmetry. In fact, with the other nucleus nearby, the potential experienced by the electron from one nucleus is not inversion symmetric (except for $\chi=90°$), leading to both *odd* and *even* harmonics in the spectra originated from a single nucleus.

In order to get an additional insight into the nuclear contributions to the harmonic spectrum, we use a Gabor analysis [20,21], which provides the time profiles of the harmonic spectra originated from each nucleus. The time profiles are obtained by taking the inverse Fourier transform of the product of $G_j(\omega)$ by a Gaussian window function, which is centered at a selected reference harmonic, and which has a specified full width at half maximum (FWHM). The resulting time profile indicates the time at which the selected set of harmonics was emitted during the pulse. Figure 6 shows the time profiles of harmonics emitted by the nuclei 1 and 2 of H_2^+ for various orientations of the molecule. The window function used to obtain these profiles is centered at the 85th harmonic and has a FWHM of $5\omega_0$. This harmonic order is near the cutoff region, where we anticipate the electron to return to the molecular core with the maximum energy $3.17U_p$ [8].

In addition, we have solved the one-dimensional (1D) classical Newton equation $\ddot{x}=-E(t)$ for the motion a free electron driven by the electric field $E(t)$ of the laser pulse. Assuming that at the initial time t_0, the electron is at the origin of the coordinates with zero velocity, we find the time of first return of the electron to the origin and the corresponding kinetic energy. These first returns are the so-called short electron trajectories [45]. By varying t_0 throughout the laser pulse, we find and plot with dots in Fig. 6(e) the first return energies versus the return time. The resulting plots shows two peaks every laser period, corresponding to two classical returns with the maximum kinetic energy $3.17U_p$

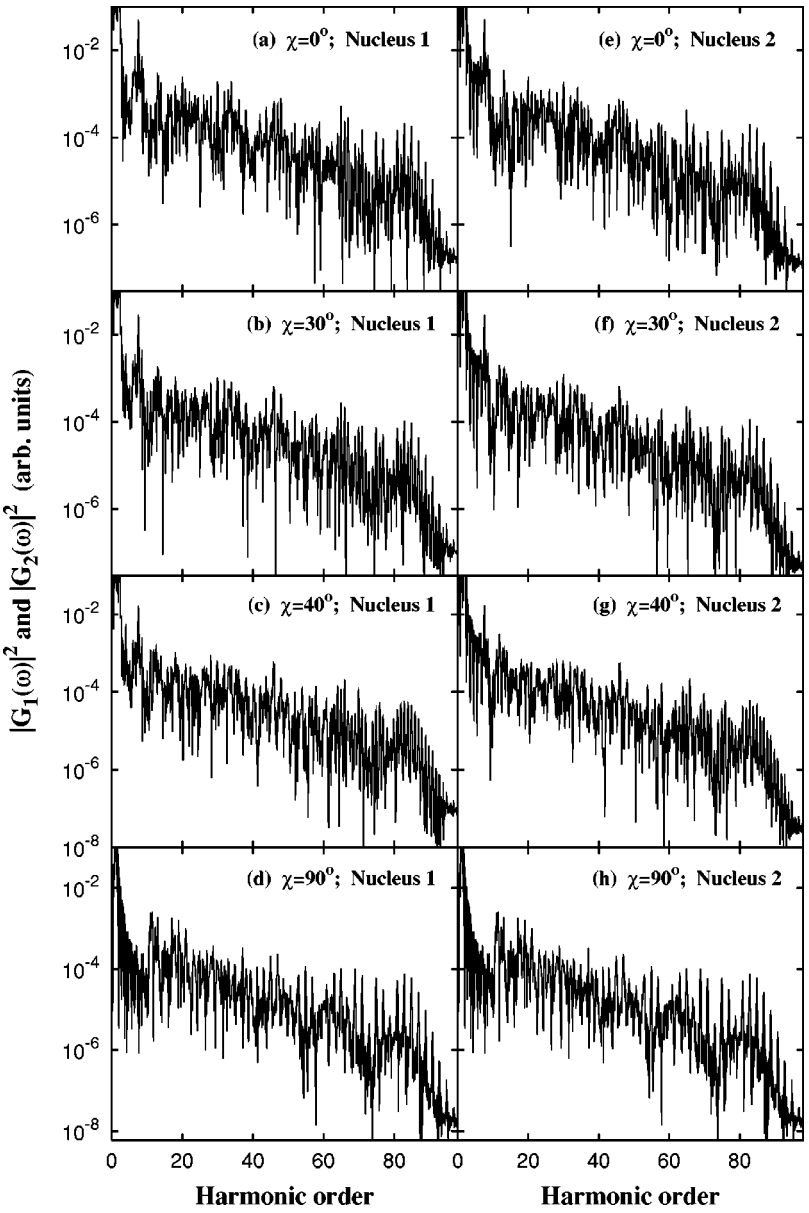

FIG. 5. Harmonic spectra (in arb. units) originating from the nucleus 1 (i.e., $|G_1(\omega)|^2$) and from the nucleus 2 (i.e., $|G_2(\omega)|^2$) of H_2^+, for various orientation angles: (a) and (e) for $\chi=0°$; (b) and (f) for $\chi=30°$; (c) and (g) for $\chi=40°$; (d) and (g) for $\chi=90°$. Plots (a), (b), (c), and (d) on the left-hand side correspond to $|G_1(\omega)|^2$, while plots (e), (f), (g), and (h) on the right-hand side correspond to $|G_2(\omega)|^2$. For $\chi=90°$, $|G_1(\omega)|^2$ and $|G_2(\omega)|^2$ are identical. The internuclear distance and laser pulse duration are the same as in Fig. 2.

[8]. Throughout the ten-cycle-long pulse used in this work, classical first returns with the maximum kinetic energy $3.17U_p$ occur at the times $t_1=-1.3$, $t_2=-0.8$, $t_3=-0.3$, $t_4=0.2$, $t_5=0.7$, $t_6=1.2$, and $t_7=1.7$ (in units of the laser periods).

For all molecular orientations, the time profiles in Fig. 6 show series of peaks separated by about half the laser period. These peaks, which indicate the instants (during the laser excitation) at which the 85th harmonic is emitted by each nucleus, agree very well with peaks in the plot of the classical first return energy versus the return time in Fig. 6(e). This indicates that high-order harmonics are indeed emitted every half-cycle by each nucleus when the electron wave packet returns for a recollision with the molecular core.

Consider Fig. 6(a) for the parallel orientation of the molecule ($\chi=0$). One sees that at the first harmonic emission at time t_1, the intensity of the time profile for the nucleus 1 is larger than that of the nucleus 2. On the other hand, the classical analysis indicates that the returning electron at time t_1 encounters nucleus 1 first, and nucleus 2 next. At the next recollision at time t_2, the returning electron encounters nucleus 2 first, then nucleus 1 next, and the intensity of the time profile at t_2 is higher for the nucleus 2 than for the nucleus 1. This asymmetry repeats itself alternatively throughout the laser pulse, with the intensity profile of the nucleus 1 dominating at one recollision and the profile of the nucleus 2 dominating a half-cycle later at the next recollision, and so on. This suggests that at each return of the electron wave packet to the molecular core, high-order harmonics are emitted predominantly by the nucleus that experiences the first recollision. Indeed, after its recollision with the first nucleus, the electron wave packet that reaches the second nucleus is diminished by its scattering and its recombination with the first nucleus. In other words, the nuclei screen each other from the returning wave packet. This is further supported by the fact that as one tends from the parallel orientation ($\chi=0°$) to the perpendicular orientation ($\chi=90°$) in Fig. 6, the asymmetry in the time profile between

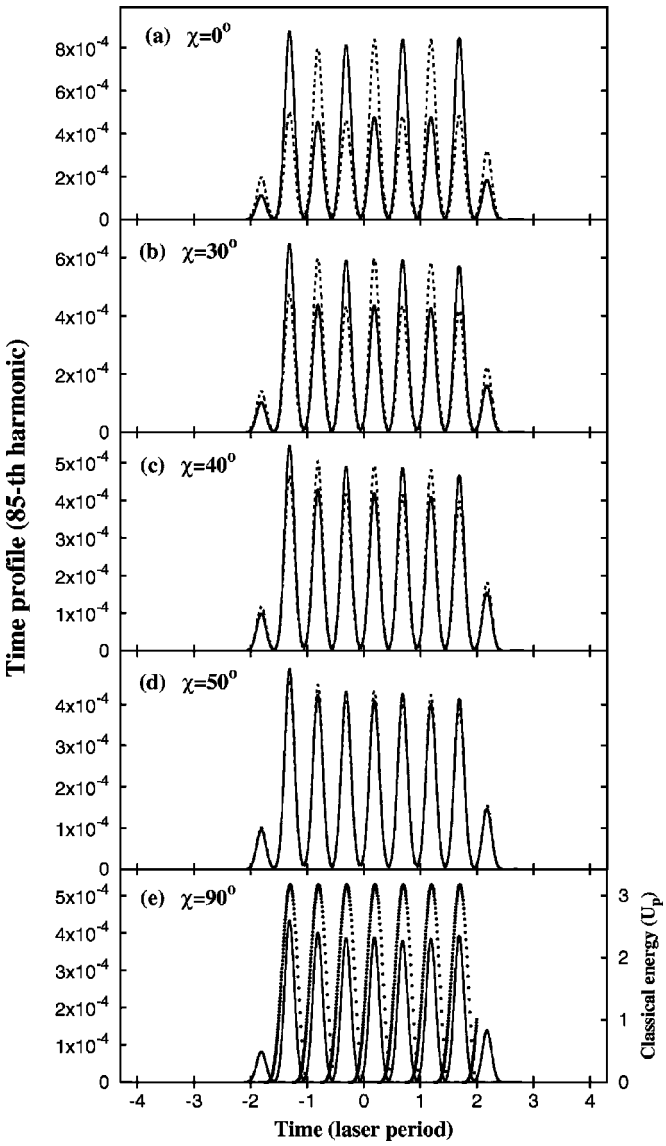

FIG. 6. Time profiles (in arb. units) of the 85th harmonic emitted by the nucleus 1 (solid lines) and by the nucleus 2 (dashed lines) of H_2^+, for laser orientation angles χ shown. In the bottom plot [(e) $\chi=90°$], where the time profiles for the two nuclei are identical, we also plot (with dots) the kinetic energy (in units of the ponderomotive energy U_p) of the returning classical electrons vs their first return times (see text for more details). Time is shown in units of the laser period.

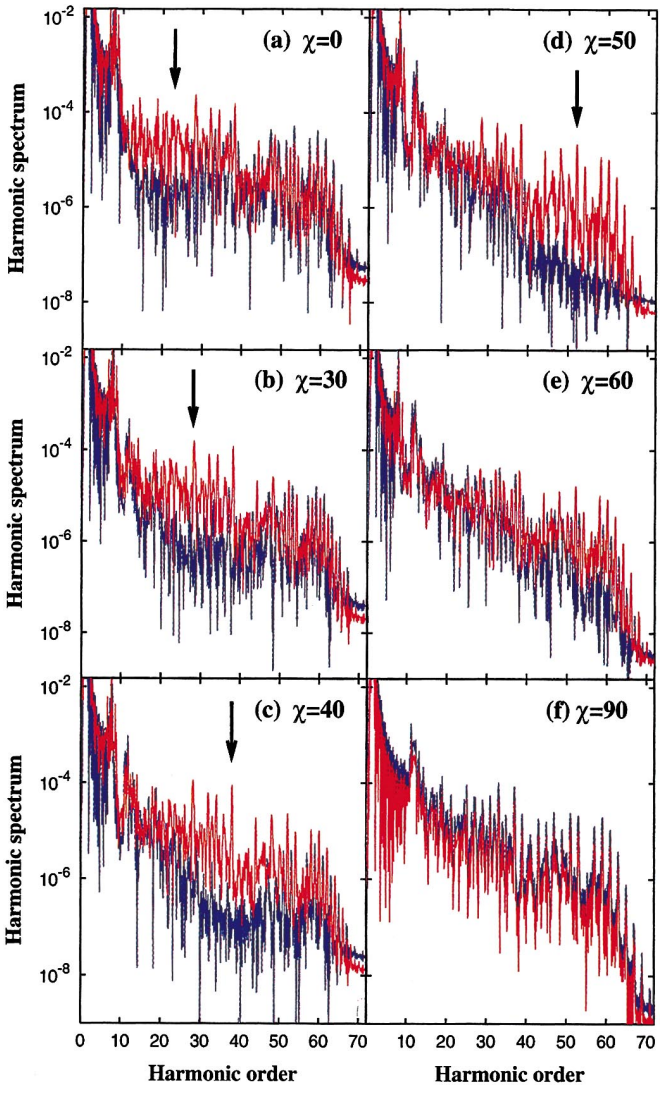

FIG. 7. (Color) Full harmonic spectrum $|G(\omega)|^2$ (blue curve) of H_2^+, and harmonic spectrum $|G_1(\omega)|^2+|G_2(\omega)|^2$ of H_2^+ without interferences (red curve). The arrows indicate the location minima due to interferences. The internuclear distance and laser pulse duration are the same as in Fig. 2. The peak intensity of the laser is $I=3\times10^{14}$ W/cm^2.

the two nuclei decreases gradually and vanishes for the case $\chi=90°$ where there is no such screening.

VI. INTERFERENCE EFFECTS IN HARMONIC GENERATION

As discussed previously, the full harmonic spectrum is almost entirely determined by $|G(\omega)|^2$, while $|G_j(\omega)|^2$ $(j=1,2)$ is the harmonic spectrum originating from the nucleus j. Since $G(\omega)=G_1(\omega)+G_2(\omega)$, then the full harmonic spectrum is given by

$$|G(\omega)|^2 = |G_1(\omega)|^2 + |G_2(\omega)|^2 + 2\,\mathrm{Re}[G_1(\omega)G_2^*(\omega)]. \tag{22}$$

It is clear that $||G_1(\omega)|^2+|G_2(\omega)|^2$ is the harmonic spectrum without interferences, and 2 Re$[G_1(\omega)G_2^*(\omega)]$ is the interference term. Therefore, plotting $|G(\omega)|^2$ and $|G_1(\omega)|^2+|G_2(\omega)|^2$ side by side provides a direct quantitative, unambiguous insight into influence of interferences in the harmonic spectra.

Plots of $|G(\omega)|^2$ and $G_1(\omega)|^2+|G_2(\omega)|^2$ for various orientations of the molecule are displayed in Fig. 7 for the peak intensity $I=3\times10^{14}$ W/cm^2, and in Fig. 8 for the peak intensity $I=5\times10^{14}$ W/cm^2. Since the harmonic spectra $|G_1(\omega)|^2$ and $|G_2(\omega)|^2$ originating from each nucleus of H_2^+ exhibit both odd and even harmonics (except for $\chi=90°$), it

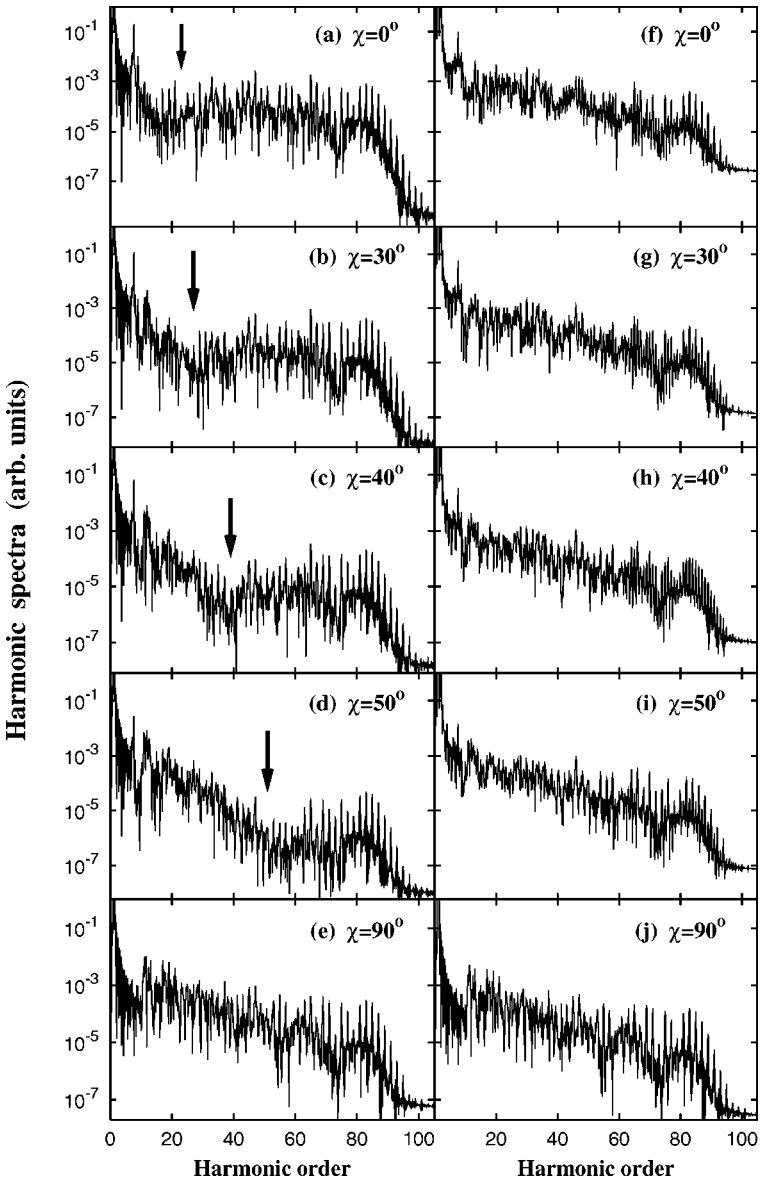

FIG. 8. Harmonic spectrum $|G(\omega)|^2$ from H_2^+ [left-hand plots: (a) for $\chi=0°$, (b) for $\chi=30°$, (c) for $\chi=40°$, (d) for $\chi=50°$, and (e) for $\chi=90°$], and harmonic spectrum $|G_1(\omega)|^2+|G_2(\omega)|^2$ from H_2^+ without interferences included [right-hand plots: (f) for $\chi=0°$, (g) for $\chi=30°$, (h) for $\chi=40°$, (i) for $\chi=50°$, and (j) for $\chi=90°$], for various angles χ shown. In each left-hand plot, the arrows point to the approximate location of a minimum induced by interferences. For $\chi=90°$, $|G(\omega)|^2=4|G_1(\omega)|^2=4|G_2(\omega)|^2$. The internuclear distance and laser pulse duration are the same as in Fig. 2. The peak intensity of the laser is $I=5\times10^{14}$ W/cm^2.

is not surprising that the harmonic spectrum of H_2^+ without interferences [see red lines in Fig. 7 and Figs. 8(f)–8(i)] also contains both odd and even harmonics. However, it appears that only odd harmonics are present in the full harmonic spectra $|G(\omega)|^2$ [see blue lines in Fig. 7 and Figs. 8(a)–8(e)], which includes interferences. In other words, interferences lead to a cancellation of even harmonics. In fact, the interference term restores the overall inversion symmetry of the system, leading to only odd harmonics.

Another interesting feature from Figs. 7 and 8 is the fact that the interference term leads to a strong suppression of a relatively broad band of consecutive harmonics, leading to a minimum in the harmonic spectrum of H_2^+. With increasing χ, the size of the band of suppressed harmonics increases, and the location of the minimum moves to higher harmonic orders. The location of these minima agrees with the interpretation in [17], where it was shown that the occurrence of minima or maxima in the harmonic spectra depends on the interference term

$$I(\mathbf{k}) = e^{i\mathbf{k}\cdot\mathbf{r}_1} + e^{i\mathbf{k}\cdot\mathbf{r}_2} = 2e^{i\mathbf{k}\cdot(\mathbf{r}_1+\mathbf{r}_2)/2}\cos\left(\frac{\mathbf{k}\cdot\mathbf{R}}{2}\right), \quad (23)$$

where $k=2\pi/\lambda$ is the electron momentum, and λ its wave number. The electron momentum $\mathbf{k}$ is polarized along the electric field, so that $\mathbf{k}\cdot\mathbf{R}=kR\cos\chi$. Destructive interference (minimum in the harmonic spectra) occurs when $I(\mathbf{k})=0$, i.e., when

$$\mathbf{k}\cdot\mathbf{R} = (2p+1)\pi, \quad p = 0,1,2,\ldots . \quad (24)$$

Similar interferences were originally pointed out in angular distributions of ATI spectra of H_2^+ [12].

The time profiles of the 85th harmonic in the spectrum of H_2^+ (including interferences) are shown in Fig. 9 for various orientation angles χ. To obtain these profiles, we use a window function centered at the 85th harmonic, with a FWHM of $5\omega_0$. In each case, the scaled electric field of the laser pulse is also plotted. For all orientation angles, the profiles show a series of peaks, which are separated by half the laser

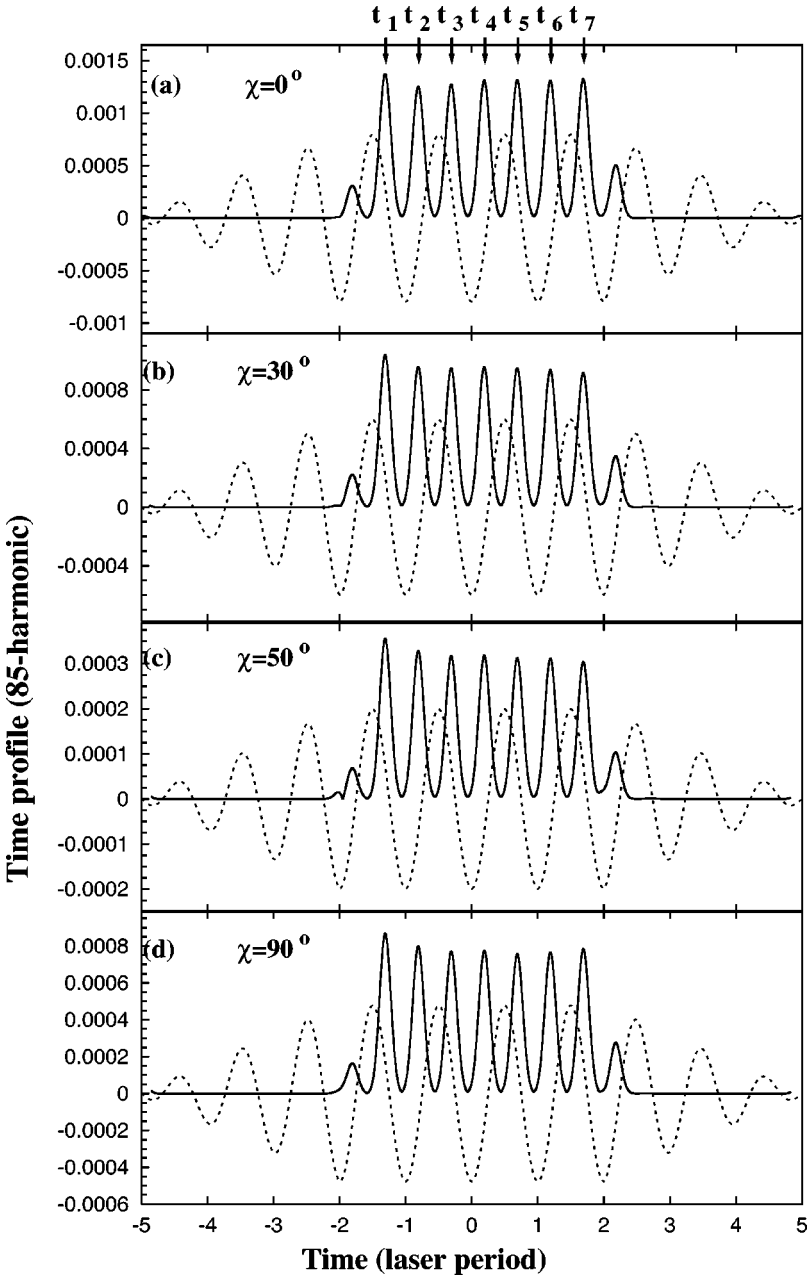

FIG. 9. Solid lines are the time profiles (arb. units) of the 85th harmonic emitted by H_2^+ for various orientations shown. Dashed lines represent the laser electric $E(t)/N$, which is divided by N to permit a comparison with the profiles [$N=150$ for (a), $N=200$ for (b), $N=600$ for (c), $N=250$ for (d)]. t_j ($j=1-7$) are the classical first return times of the electron with the maximum kinetic energy $3.17U_p$, as described in the text. Time is in units of the laser period. The internuclear distance and laser pulse duration are the same as in Fig. 2. The peak intensity of the laser is $I=5\times10^{14}$ W/cm^2.

period, and which coincide with the classical first return times t_j ($j=1,7$) described earlier. This means that such high-order harmonics are emitted when the electron returns for a recollision with the molecular core, in agreement with the semiclassical recollision mechanism. The emission occurs predominantly when the peak of the laser pulse is reached, at intensities where tunnelling is significant. One also sees that harmonic emission occurs in the vicinity of the zeros of the electric field, independently of the molecular orientation. This is in agreement with the semiclassical recollision model [8].

Further insight into the interference resulting from electron recollision with the molecular ion core is gained from a time profile analysis of the harmonic spectra of H_2^+ in the vicinity of the interference minima shown in Fig. 8. Explicitly, we use a window function centered at the interference minima with a FWHM of $5\omega_0$ as in Figs. 6 and 9. The profiles of the full harmonic emission of H_2^+, as well as those of harmonic emissions from each nucleus, are shown in Fig. 10, with the scaled electric field of the laser superimposed. For all orientations shown in Fig. 10, one sees that due to destructive interference, the profiles for the full harmonic spectrum of H_2^+ (with interferences included) are significantly suppressed compared to the profiles for each nucleus. The 85th harmonic at $\chi=60°$ [Fig. 10(d)] is located near the cutoff harmonic energy given by Eq. (1), and corresponds to a classical recollision trajectory without the Coulomb potential, the so-called short trajectory [46]. Figure 10(d) indicates that the 85th harmonic at $\chi=60°$ is emitted near the zero of the electric field. In this cutoff energy region, indeed, harmonic emission always occur at the zero of the electric field of the laser, when electrons following short trajectories return to the molecular core. This is confirmed in Fig. 9 for all orientation angles.

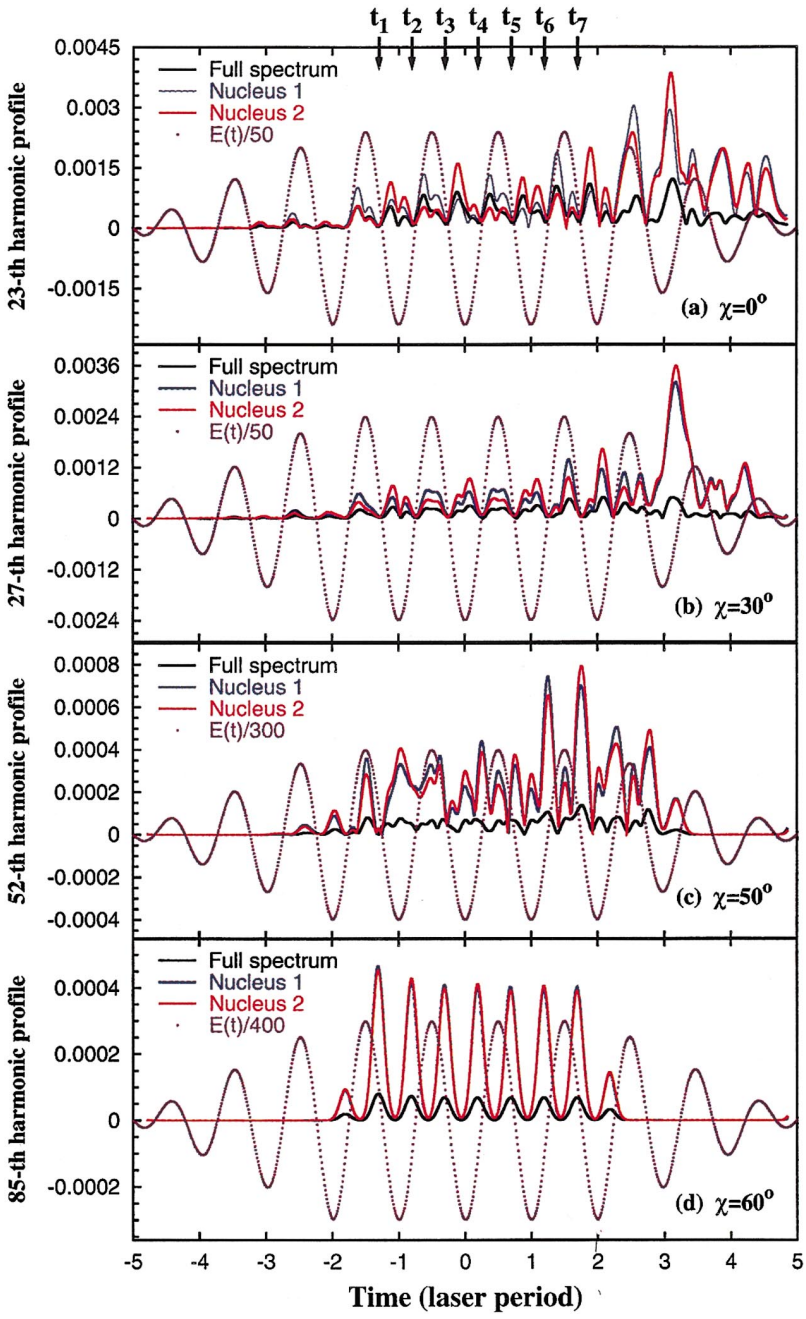

FIG. 10. (Color) Time profiles (in arb. units) for harmonic orders in the vicinity of interference minima in the spectra of H_2^+ (see Fig. 8) for the peak intensity $I=5\times10^{14}$ W/cm^2. The following are plotted for orientation angles χ shown: the scaled electric field (magenta dots), the time profiles of the full harmonic spectrum of H_2^+ with interferences included (black lines), the time profiles of harmonic spectra originating from the nucleus 1 (blue lines) and from the nucleus 2 (red lines). The instants t_j ($j=1-7$) are the classical times of first electron return as described in Fig. 9.

However, photon emission for harmonics at the interference minima for other orientation angles [see Figs. 10(a)–10(c)] show the occurrence of harmonic emission at times that do not correspond to short trajectories. The semiclassical recollision model predicts that at lower energies, i.e., lower harmonics, two recollision trajectories should dominate, coalescing into one single trajectory at the maximum cutoff energy [46,47]. Thus, at lower energies, one extra trajectory, called the long trajectory, is expected to return to the molecular core at the peak of the electric field. This extra trajectory has been recently characterized [45]. Figure 10 illustrates quantitatively this semiclassical prediction, as the profiles indicate harmonic emission (recollisions) occurring near the maxima (minima) and the zeros of the electric field for harmonics well below the cutoff [see Figs. 10(a)–10(c)]. Note that for double trajectories (low-order harmonics) and single trajectories (high-order harmonics), efficient destructive interference is seen to occur, reflecting the fact that photon emission amplitudes at each nucleus are out of phase with each other. Next, we examine the theoretical formulations that allow to elucidate these multicenter interference phenomena, which occur only in molecules and which have already been predicted to occur in molecular ATI spectra [12].

VII. ACCELERATION VERSUS DIPOLE PHOTON EMISSION

It has been shown that the correct evaluation of the harmonic spectrum is to proceed via the Fourier transform $\mathbf{A}(\omega)$

of the acceleration of the dipole, which may be expressed as [24]

$$\mathbf{A}(\omega) = \int_0^T e^{i\omega t}\ddot{\mathbf{d}}(t)dt$$

$$= -i\omega e^{i\omega T}\mathbf{d}(T) + e^{i\omega T}\dot{\mathbf{d}}(T) - \omega^2\int_0^T e^{i\omega t}\mathbf{d}(t)dt, \quad (25)$$

where $\mathbf{d}(t)=\langle\Psi(t)|(-\mathbf{r})|\Psi(t)\rangle$ is the mean dipole moment of the electron, and $\Psi(t)$ the exact time-dependent wave function at time t. For simplicity, the turnon of the laser pulse is chosen at $t=0$, and its turnoff at $t=T$. Exploiting Ehrenfest's theorem, $\mathbf{A}(\omega)$ can be expressed as in Eq. (18) in terms of the gradient of the Coulomb potential [24]. It is quite common [46] to evaluate the harmonic spectrum using the Fourier transform of the dipole moment $\mathbf{D}(\omega)=-\omega^2\int_0^T e^{i\omega t}\mathbf{d}(t)dt$, i.e., the last term in Eq. (25). Clearly, expressions of $\mathbf{A}(\omega)$ and $\mathbf{D}(\omega)$ are equivalent if $\dot{\mathbf{d}}(T)$ and $\mathbf{d}(T)$ vanish at the end of the pulse, and if an exact wave function $\Psi(t)$ is used. Using $\mathbf{A}(\omega)$ (the acceleration form) emphasizes maximum acceleration at the nuclei, whereas using $\mathbf{D}(\omega)$ (the dipole form) emphasizes the spatial extent of electron trajectories. Below, we analyze the two forms in the context of an approximate wave function $\Psi(t)$, and compare with our exact numerical calculations.

We start by approximating the time-dependent wave function by a superposition of the ground-state wave function Ψ_0, and a continuum wave packet Ψ_c, which describes the recombining electron [46],

$$\Psi(\mathbf{r},t) = \beta(t)e^{-iE_0t}\Psi_0(\mathbf{r}) + \Psi_c(\mathbf{r},t). \quad (26)$$

$E_0=-I_p$ is the ground-state energy, and $\beta(t)$ is the ground-state probability amplitude. We assume that there is little depletion of the initial state, so that $\beta(t)\approx 1$. For a single recollision event, Ehrenfest's theorem gives

$$A(\omega) = \int e^{iE_0t}\langle\Psi_0|\mathbf{e}\cdot\nabla V(r)|\Psi_c(t)\rangle e^{i\omega t}dt + \text{c.c.}, \quad (27)$$

after neglecting terms involving continuum-continuum transitions, and after ignoring the term that involves the electric field $E(t)$ as for Eq. (19).

We approximate the initial state wave function by a linear combination of atomic orbitals (LCAO) [12,48]

$$\Psi_0^{\pm} = N_0^{\pm}(e^{-\alpha_{\pm}r_1} \pm e^{-\alpha_{\pm}r_2}), \quad (28)$$

where $N_0^{\pm}$ is a normalization constant. We assume that the initial state could have a gerade $(+)$ or ungerade $(-)$ symmetry. The real parameter $\alpha_{\pm}$ can be adjusted so that the energy associated with the wave function (28) agrees with the exact energy of ground or first excited state of H_2^+ [48,49]. The continuum wave function describing the electron returning to the molecular core with energy $k^2/2$ is approximated by the plane wave

$$\Psi_c(t) = e^{i(\mathbf{k}\cdot\mathbf{r}-E_{\mathbf{k}}t)}. \quad (29)$$

This leads to

$$A^{\pm}(\omega) = N_0^{\pm}Z\delta(E_0 - E_{\mathbf{k}} + \omega)\int d\mathbf{r}(e^{-\alpha_{\pm}r_1} \pm e^{-\alpha_{\pm}r_2})$$

$$\times\left(\frac{\mathbf{e}\cdot\mathbf{r}_1}{r_1^3} + \frac{\mathbf{e}\cdot\mathbf{r}_2}{r_2^3}\right)e^{i\mathbf{k}\cdot\mathbf{r}} + \text{c.c.} \quad (30)$$

Consider the integral

$$\int e^{-\alpha r_1}\left(\frac{\mathbf{e}\cdot\mathbf{r}_1}{r_1^3} + \frac{\mathbf{e}\cdot\mathbf{r}_2}{r_2^3}\right)e^{i\mathbf{k}\cdot\mathbf{r}}d\mathbf{r}. \quad (31)$$

The quantity $e^{-\alpha r_1}=e^{-\alpha|\mathbf{r}+\mathbf{R}/2|}$ is maximum at $r_1=0$ (i.e., at $\mathbf{r}=-\mathbf{R}/2$), and is negligible elsewhere. $\mathbf{e}\cdot\mathbf{r}_1/\mathbf{r}_1^3$ is also maximum at $\mathbf{r}=-\mathbf{R}/2$, while $\mathbf{e}\cdot\mathbf{r}_2/\mathbf{r}_2^3$ is maximum at $r_2=0$ (i.e., at $\mathbf{r}=\mathbf{R}/2$), where $e^{-\alpha r_1}=e^{-\alpha|\mathbf{r}+\mathbf{R}/2|}$ is negligible (provided that R is relatively large). Therefore, the second term in Eq. (31) is negligible compared to the first one, so that

$$\int e^{-\alpha r_1}\left(\frac{\mathbf{e}\cdot\mathbf{r}_1}{r_1^3} + \frac{\mathbf{e}\cdot\mathbf{r}_2}{r_2^3}\right)e^{i\mathbf{k}\cdot\mathbf{r}}d\mathbf{r} \approx \int e^{-\alpha r_1}\frac{\mathbf{e}\cdot\mathbf{r}_1}{r_1^3}e^{i\mathbf{k}\cdot\mathbf{r}}d\mathbf{r}. \quad (32)$$

Similarly, one can show that

$$\int e^{-\alpha r_2}\left(\frac{\mathbf{e}\cdot\mathbf{r}_1}{r_1^3} + \frac{\mathbf{e}\cdot\mathbf{r}_2}{r_2^3}\right)e^{i\mathbf{k}\cdot\mathbf{r}}d\mathbf{r} \approx \int e^{-\alpha r_2}\frac{\mathbf{e}\cdot\mathbf{r}_2}{r_2^3}e^{i\mathbf{k}\cdot\mathbf{r}}d\mathbf{r}. \quad (33)$$

This gives

$$A^{\pm}(\omega) = N_0^{\pm}Z\delta(E_0 - E_{\mathbf{k}} + \omega)$$

$$\times\left\{\int e^{-\alpha_{\pm}r_1}\frac{\mathbf{e}\cdot\mathbf{r}_1}{r_1^3}e^{i\mathbf{k}\cdot\mathbf{r}}d\mathbf{r} \pm \int e^{-\alpha_{\pm}r_2}\frac{\mathbf{e}\cdot\mathbf{r}_2}{r_2^3}e^{i\mathbf{k}\cdot\mathbf{r}}d\mathbf{r}\right\}$$

$$+ \text{c.c.} = N_0^{\pm}Z\delta(E_0 - E_{\mathbf{k}} + \omega)[e^{-i\mathbf{k}\cdot\mathbf{R}/2} \pm e^{i\mathbf{k}\cdot\mathbf{R}/2}]$$

$$\times\int e^{-\alpha_{\pm}r}\frac{\mathbf{e}\cdot\mathbf{r}}{r^3}e^{i\mathbf{k}\cdot\mathbf{r}}d\mathbf{r} + \text{c.c.}, \quad (34)$$

after making a change of variables $\mathbf{r}\rightarrow\mathbf{r}_1$ and $\mathbf{r}\rightarrow\mathbf{r}_2$. The above equation clearly exhibits the more general interference term $(e^{-i\mathbf{k}\cdot\mathbf{R}/2}\pm e^{i\mathbf{k}\cdot\mathbf{R}/2})$, where the $+$ and $-$ signs correspond to the gerade and ungerade initial states, respectively. For the initial ground state of H_2^+ (gerade) involved in this work, one retrieves the interference term $I(\mathbf{k})$ given by Eq. (23). Such an interference was originally obtained in ATI spectra in H_2^+ [12].

Let N_{min} be the harmonic order corresponding to a minimum in the harmonic spectrum of H_2^+, the energy of the harmonic photon corresponding to this minimum is $N_{min}\omega_0$. If $\mathbf{k}$ is the electron momentum at the instant of recombination of the electron wave packet with the ground state, then we may write

$$\frac{1}{2}\mathbf{k}^2 = N_{min}\omega_0. \quad (35)$$

Note that we consider Eq. (35), instead of $\frac{1}{2}\mathbf{k}^2=I_p+N_{min}\omega_0$, which explicitly contains the ionization potential I_p of the molecule, and which naturally emerges from Eq. (34). The reason for this is that the recollision occurs near the nuclei,

TABLE II. Harmonic order at which an interference minimum occurs in the harmonic spectrum of H_2^+ for various orientation angles χ. Results from the solution of the TDSE (second column) are compared with those obtained from the acceleration formula given by Eq. (23) using $I(\mathbf{k})=0$ (third column), and with those derived from the dipole formula given by Eq. (43) using $\mathcal{I}(\mathbf{k})=0$ (fourth column).

	Harmonic order N_{min} at the minimum		
Angle χ	TDSE (This work)	Acceleration +LCAO	Exact Dipole +LCAO
0	≈23	22	42
30	≈27	29	55
40	≈39	37	68
45	≈43	43	79
50	≈51	52	95
60	≈cutoff	87	153
75	>cutoff	323	553
90	None	∞	∞

when the electron momentum $\mathbf{k}$ in Eq. (35) already encompasses the effect of the Coulomb potential. Obtaining $\mathbf{k}$ from the destructive interference condition given by Eq. (24), one can use Eq. (35) to derive the harmonic order $N_{\min}$ at which a minimum in the harmonic spectrum is expected.

For various orientation angles, we summarize in Table II the harmonic orders N_{min} at which a minimum occurs in the harmonic spectra of H_2^+. The second column in Table II contains the harmonic orders obtained in this work, after solution of the TDSE (see arrows in Figs. 7 and 8). The harmonic order in the third column are obtained by using Eqs. (24) and (35) as described above ("acceleration" values). It appears that results from the solution of the TDSE agree quite well with "acceleration" values. This indicates that the simple emission model from a continuum to a bound state via an acceleration mechanism arising from electron recollision reproduces the interference pattern quite well. Note, however, that the minima obtained in Figs. 7 and 8 from the full 3D time TDSE are rather broad, suggesting that many electron trajectories with different momenta actually contribute to each minimum.

We examine next the transition matrix element T_H, which determines the intensity of the HOHG spectrum. Consider the multiphoton transition from the initial electronic state $|0\rangle$ to a continuum state $|k\rangle$ and then back to the same initial ground state by emission of a photon of energy $E=N\omega$. The transition matrix element can be considered as a hyper-Raman process through the continuum state $|k\rangle$ and is written as [22]

$$\langle 0|T_H|0\rangle = \int_{\lim\ \epsilon\to 0} dE_k \frac{\langle 0|T_N|k\rangle\langle k|d|0\rangle}{E-E_k+i\epsilon} \tag{36}$$

$$= \mathrm{P}\int dE_k \frac{\langle 0|T_N|k\rangle\langle k|d|0\rangle}{E-E_k} - i\pi\delta(E-E_k)\langle 0|T_N|k\rangle\langle k|d|0\rangle, \tag{37}$$

where the integral sums over all intermediate continuum states $|k\rangle$. The total harmonic transition matrix element of T_H is separated into a nonresonant principal part (P) integral and a resonant transition $E=E_k$, where E is the initial (final) total energy of the laser-molecule system. T_N is an (unknown) intermediate transition operator corresponding to the multiphoton transition from the initial bound state $|0\rangle$ to the continuum state $|k\rangle$ from which photon emission occurs. In Eq. (37), we have emphasized the dipole form of the photon emission process. For continuum energies E_k much larger than the ionization potential I_p, which is the threshold energy for continuum excitation, the PP integral becomes negligible due to cancellation from fluctuations of the denominator: $E-E_k>0$ and $E-E_k<0$ in Eq. (36). Only in this limit can we assume that the total transition moment depends on the resonant process, i.e.,

$$\langle 0|T_H|0\rangle \propto \langle k|d|0\rangle. \tag{38}$$

The absolute phase of Eq. (36) is an essential factor in attosecond pulse synthesis [50] and depends on both nonresonant and resonant contributions.

Note, however, that instead of the acceleration formula of Eq. (27), one could use the traditional dipole formula

$$D(\omega) = \int e^{iE_0 t}\langle\Psi_0|\mathbf{e}\cdot\mathbf{r}|\Psi_c(t)\rangle e^{i\omega t}dt + \text{c.c.}, \tag{39}$$

which involves the transition matrix (38). Interestingly, using the wave functions (28) and (29), the above integral can be evaluated exactly, without using the approximations described earlier in the evaluation of the integral (27). Indeed,

$$\begin{aligned} D^{\pm}(\omega) &= \int e^{i(E_0-E_{\mathbf{k}}+\omega)t}dt \\ &\quad\times \int N_0^{\pm}(e^{-\alpha_{\pm}r_1}\pm e^{-\alpha_{\pm}r_2})\mathbf{e}\cdot\mathbf{r}e^{i\mathbf{k}\cdot\mathbf{r}}d\mathbf{r} + \text{c.c.} \\ &= N_0^{\pm}\delta(E_0-E_{\mathbf{k}}+\omega) \\ &\quad\times \int (e^{-\alpha_{\pm}r_1}\pm e^{-\alpha_{\pm}r_2})\mathbf{e}\cdot(-i\nabla_{\mathbf{k}})e^{i\mathbf{k}\cdot\mathbf{r}}d\mathbf{r} + \text{c.c.} \\ &= -iN_0^{\pm}\delta(E_0-E_{\mathbf{k}}+\omega)\mathbf{e}\cdot\nabla_{\mathbf{k}}\{(e^{-i\mathbf{k}\cdot\mathbf{R}/2}\pm e^{i\mathbf{k}\cdot\mathbf{R}/2})\Phi_{1s}^{\pm}(\mathbf{k})\} \\ &\quad + \text{c.c.}, \end{aligned} \tag{40}$$

where

$$\Phi_{1s}^{\pm}(\mathbf{k}) = \int e^{-\alpha_{\pm}r}e^{i\mathbf{k}\cdot\mathbf{r}}d\mathbf{r} = \frac{8\pi\alpha_{\pm}}{(\alpha_{\pm}^2+\mathbf{k}^2)^2} \tag{41}$$

is the Fourier transform of the atomic orbital $e^{-\alpha_{\pm}r}$. For the case of a gerade (+) ground state considered in this work, one obtains

$$D^{+}(\omega) = -2iN_0\delta(\omega-E_{\mathbf{k}})\Phi_{1s}^{+}(\mathbf{k})\mathcal{I}(\mathbf{k}), \tag{42}$$

where $\mathcal{I}(\mathbf{k})$ is given by

$$\mathcal{I}(\mathbf{k}) = \frac{\mathbf{e}\cdot\mathbf{R}}{2}\sin\left(\frac{\mathbf{k}\cdot\mathbf{R}}{2}\right) + \frac{4\mathbf{e}\cdot\mathbf{k}}{\alpha_{\pm}^2 + k^2}\cos\left(\frac{\mathbf{k}\cdot\mathbf{R}}{2}\right). \quad (43)$$

Imposing the destructive interference condition $\mathcal{I}(\mathbf{k})=0$, one arrives at discrete numerical solution that depends on an integer p as in Eq. (24). The resulting harmonics orders at which minima are predicted are given in the fourth column of Table II. These results do not agree with our time-dependent calculations in the second column, as well as with the predictions of the interference term $I(\mathbf{k})$ obtained from the acceleration form. This means that obtaining the harmonic spectrum via the dipole fails to predict interference effects correctly, when a LCAO wave function and a plane wave are used to represent the ground-state wave function Ψ_0 and the continuum wave function Ψ_c, respectively. The acceleration form emphasizes maximum acceleration near the nuclei (short distances), thus, intuitively, the acceleration form more accurately reproduces the two-center character of the molecule, in contrast to the dipole form that emphasizes the spatial extent (large distances) of electron trajectories. Since the two forms are equivalent when exact wave functions are used, the failure of the dipole form is due to the use of approximate wave functions Ψ_0 and Ψ_c. Using a Coulomb two-center continuum wave function instead of a plane wave could improve results for the dipole form. We note that the free electron states e^{ikr} are not orthogonal to the initial state LCAO wave functions (28), and thus can give spurious results [51].

VIII. CONCLUSIONS

We have described a new accurate method for solving the 3D TDSE for a two-center molecule in interaction with an intense laser field having an arbitrarily oriented linear polarization. The method uses spheroidal coordinates and expands the time-dependent wave function in a basis of associated Laguerre and Legendre functions. We show that projecting the TDSE in the basis of electronic eigenstates allows to exploit additional symmetry, resulting in a significant speedup of calculations. Complex scaling is used to prevent the electron probability flux from reflecting when it eventually reaches the boundaries of the region described by our wave function.

A good agreement is found between results obtained in the length and velocity gauges. Our results show that the ionization probability of H_2^+ is maximum for the parallel orientation of the molecule with respect to the laser field polarization, and decreases to reach a minimum for the perpendicular orientation. The harmonic spectra originating from each nucleus indicates that each nucleus is a source of harmonic radiation, which has all features relevant to the harmonic spectrum emitted by an atom, except that both odd and even harmonics appear in the spectrum. A time-profile analysis of the harmonic spectra emitted by each nucleus indicates that the emission of high-order harmonics by each nucleus occurs every half-cycle when the electron wave packet returns for a recollision with the molecular core. We have also calculated the harmonic spectra of H_2^+ with and without interferences included. We confirm that the harmonic spectrum of H_2^+ exhibits minima, which are explicitly shown to be due to interferences.

A simple interpretation of interference effects in the harmonic spectrum of H_2^+ can be obtained via a transition matrix coupling the ground state described approximately by a linear combination of atomic orbitals (LCAO) and a continuum state described approximately by a plane wave. The acceleration and dipole forms of the transition matrix lead to different results due to the use of approximate ground and/or continuum wave functions. We have shown that the acceleration form predicts accurately the interference effects in H_2^+, while the dipole form does not. The accuracy of the acceleration form is related to the fact that it weights the short range (harmonics are emitted at these short distances) part of the wave functions more highly than the dipole form, which emphasizes larger distances. Using a plane wave to describe the continuum state Ψ_c, the dipole form of the transition matrix indicates that the emission of harmonic photons is proportional to the Fourier transform of the ground-state wave function Ψ_0 [see Eq. (39)]. This feature is a key ingredient of a recent method for tomographic imaging of the ground-state molecular orbitals [25], a method that exploits the orientation dependence of HOHG spectra discussed in this paper. Our work emphasizes that a formulation of tomographic imaging based on the acceleration form (instead of the dipole form as in Ref. [25]) could be more accurate in reconstructing molecular orbitals from the harmonic spectrum. One final issue is the phase variation of the HOHG amplitudes at the intensity minima illustrated in Figs. 7 and 8, and observed in model calculations [17]. It has been suggested that this is due to a resonance effect where the recolliding electron wavelength is commensurate with the internuclear distance as indicated by Eqs. (23) and (24). Clarification of these issues will help develop HOHG in molecules as a new tool for electron imaging and new sources of attosecond pulse synthesis [3].

ACKNOWLEDGMENTS

We thank NSERC (Natural Science and Engineering Research Council of Canada) and CIPI (Canadian Institute for Photonic Inovation) for financing this research. We also acknowledge illuminating discussions with our colleagues, P.B. Corkum, D. Villeneuve, and S. Chelkowski.

APPENDIX A: OVERLAP AND ELECTRONIC HAMILTONIAN OF MATRIX ELEMENTS

For any operator $\hat{X}$, the matrix elements are given by

$$X_{\rho}^{\rho'} = \int d\tau\, U_{\nu'}^{m'}(\xi) V_{\mu'}^{m'}(\eta) \hat{X} U_{\nu}^{m}(\xi) V_{\mu}^{m}(\eta) \frac{e^{i(m-m')\phi}}{2\pi}, \quad (A1)$$

where ρ and ρ' denote the sets of parameters $\{m,\mu,\nu\}$ and $\{m',\mu',\nu'\}$, respectively. $\hat{X}$ is the unit operator for the case of the overlap matrix $\mathbf{S}$, and $\hat{X}=H$ for the matrix $\mathbf{H}$. $d\tau = \frac{1}{8}R(\xi^2-\eta^2)d\xi\, d\eta\, d\phi$ is the volume element in spheroidal

coordinates. Therefore, the overlap and atomic Hamiltonian matrix elements can be written respectively as

$$S_\rho^{\rho'} = \delta_{m',m}\frac{R^3}{8}[d^m_{\nu',\nu}(2)\tilde{d}^m_{\mu',\mu}(0) - d^m_{\nu',\nu}(0)\tilde{d}^m_{\mu',\mu}(2)], \tag{A2}$$

$$H_\rho^{\rho'} = -\delta_{m',m}\frac{R}{4}[h^m_{\nu',\nu}\tilde{d}^m_{\mu',\mu}(0) + d^m_{\nu',\nu}(0)\tilde{h}^m_{\mu',\mu}]. \tag{A3}$$

The nuclei repulsion is not included in the above matrix elements of H. Quantities involved in these expressions are given by

$$d^m_{\nu',\nu}(q) = \int_1^\infty U^m_{\nu'}(\xi)U^m_\nu(\xi)\xi^q\, d\xi, \tag{A4}$$

$$\tilde{d}^m_{\mu',\mu}(q) = \int_{-1}^{+1} V^m_{\mu'}(\eta)V^m_\mu(\eta)\,\eta^q\, d\eta, \tag{A5}$$

$$h^m_{\nu',\nu} = \int_1^\infty U^m_{\nu'}(\xi)\left[\frac{\partial}{\partial\xi}\left((\xi^2-1)\frac{\partial}{\partial\xi}\right) - \frac{m^2}{\xi^2-1} + 2ZR\xi\right]U^m_\nu(\xi)d\xi, \tag{A6}$$

$$\tilde{h}^m_{\mu',\mu} = \int_{-1}^1 V^m_{\mu'}(\eta)\left[\frac{\partial}{\partial\eta}\left((1-\eta^2)\frac{\partial}{\partial\eta}\right) - \frac{m^2}{1-\eta^2}\right]V^m_\mu(\eta)d\eta, \tag{A7}$$

where q is a non-negative integer, and $\delta_{m',m}$ is the Kronecker symbol that gives rise to the selection rule $m'=m$ in **S** and **H**. Note that we denote all integrals involving the variable η with a tilde, and those involving the variable ξ without a tilde.

Using the expression of $U^m_\nu(\xi)$ given by Eq. (7) and change of variable $X=2\alpha(\xi-1)$, one obtains

$$d^m_{\nu',\nu}(q) = \frac{N^m_{\nu'}N^m_\nu}{2\alpha}\int_0^\infty e^{-X}\left(\frac{X}{2\alpha}+1\right)^q\left(\frac{X^2}{4\alpha^2}+\frac{X}{\alpha}\right)^{|m|} \times L^{2|m|}_{\nu'-m}(X)L^{2|m|}_{\nu-m}(X)dX. \tag{A8}$$

We evaluate the integral in Eq. (A8) numerically using the Gauss-Laguerre quadrature formula [52]

$$\int_0^\infty e^{-X}f(X)dX = \sum_{j=1}^N w_j\, f(X_j), \tag{A9}$$

where w_j and X_j are the weights and abscissae, respectively, of the Gauss-Laguerre quadrature. Note that when $f(X)$ is a polynomial, as is the case in Eq. (A8), the Gauss-Laguerre quadrature (A9) is exact, provided that the number of quadrature points N is larger than half the degree of the polynomial $f(x)$ [52].

Using Eq. 8.971.3 of [28], one can show that

$$\frac{\partial}{\partial\xi}L^{2|m|}_{\nu-|m|}[2\alpha(\xi-1)] = \frac{\nu-|m|+1}{\xi-1}L^{2|m|}_{\nu-|m|+1}[2\alpha(\xi-1)] - \frac{\nu+|m|+1-2\alpha(\xi-1)}{\xi-1} \times L^{2|m|}_{\nu-|m|}[2\alpha(\xi-1)]. \tag{A10}$$

Exploiting the recurrence (A10), the action of the derivative operator in square-bracket in Eq. (A6) on $U^m_\nu(\xi)$ can be expressed in terms of Laguerre polynomials as $\Sigma^2_{n=0}A_n(\xi)L^{2|m|}_{\nu-|m|+n}[2\alpha(\xi-1)]$, where the $A_n(\xi)$'s are a mixture of polynomials and rational functions of ξ, and where $n=0,1,2,\ldots$. Thus, the integral in Eq. (A6) can be written as a sum of integrals of a product of $A_n(\xi)$ by two Laguerre polynomials [i.e., integrals similar to Eq. (A8)], which we also evaluate numerically using the Gauss-Laguerre quadrature.

From the recurrence relations of associated Legendre functions [28], one can show that

$$\eta V^m_\mu(\eta) = \sqrt{\frac{(\mu-m+1)(\mu+m+1)}{(2\mu+1)(2\mu+3)}}V^m_{\mu+1}(\eta) + \sqrt{\frac{(\mu-m)(\mu+m)}{(2\mu-1)(2\mu+1)}}V^m_{\mu-1}(\eta). \tag{A11}$$

In order to evaluate $d^m_{\nu',\nu}(q)$, we iteratively apply the recurrence relation (A11) to express $\eta^q V^m_\mu(\eta)$ as $\Sigma_n B_n(\mu,m)V^m_{\mu\pm n}(\eta)$, where the $B_n(\mu,m)$'s depend on the quantum numbers μ and m but not on η, and where $n=0,1,2,\ldots$. Then we use the fact that

$$\int_{-1}^{+1} V^m_{\mu'}(\eta)V^m_\mu(\eta)d\eta = \delta_{\mu',\mu}. \tag{A12}$$

In this way, the integrals $\tilde{d}^{m',m}_{\mu',\mu}(q)$ up to $q=3$ needed in this work are obtained in closed analytical form. Since the resulting expressions are quite bulky, we do not reproduce them in this paper.

Starting from the first-order differential equation defining Legendre polynomials $P^m_\mu(\eta)$ (see, e.g., Eq. 8.700.1 of Ref. [28]) one can show that $V^m_\mu(\eta)$ satisfies

$$\left[\frac{\partial}{\partial\eta}\left((1-\eta^2)\frac{\partial}{\partial\eta}\right) - \frac{m^2}{1-\eta^2}\right]V^m_\mu(\eta) = -\mu(\mu+1)V^m_\mu(\eta). \tag{A13}$$

This gives

$$\tilde{h}^m_{\mu',\mu} = -\mu(\mu+1)\delta_{\mu,\mu}. \tag{A14}$$

APPENDIX B: DIPOLE MATRIX ELEMENTS

In the length gauge, dipole matrix elements are given by Eq. (A1), with $\hat{X}=y=(R/2)\sin\phi\sqrt{(\xi^2-1)(1-\eta^2)}$ and $\hat{X}=z=(R/2)\xi\eta$ for the y and z components of the dipole, respectively [27]. This leads to

$$(D_y^L)_\rho^{\rho'} = \frac{(\delta_{m',m+1} - \delta_{m',m-1})}{2i}\frac{R^4}{2^4} \times\{t_{\nu',\nu}^{m',m}(2)\tilde{t}_{\mu',\mu}^{m',m}(0) - t_{\nu',\nu}^{m',m}(0)\tilde{t}_{\mu',\mu}^{m',m}(2)\} \quad \text{(B1)}$$

for the y component of the dipole in the length gauge, and

$$(D_z^L)_\rho^{\rho'} = \delta_{m',m}\frac{R^4}{2^4}\{d_{\nu',\nu}^{m}(3)\tilde{d}_{\mu',\mu}^{m}(1) - d_{\nu',\nu}^{m}(1)\tilde{d}_{\mu',\mu}^{m}(3)\} \quad \text{(B2)}$$

for the z component of the dipole in the length gauge, where

$$t_{\nu',\nu}^{m',m}(q) = \int_1^\infty U_{\nu'}^{m'}(\xi)U_\nu^m(\xi)\xi^q\sqrt{\xi^2-1}\,d\xi, \quad \text{(B3)}$$

$$\tilde{t}_{\mu',\mu}^{m',m}(q) = \int_{-1}^{+1} V_{\mu'}^{m'}(\eta)V_\mu^m(\eta)\eta^q\sqrt{1-\eta^2}\,d\eta, \quad \text{(B4)}$$

with q as an integer. $d_{\nu',\nu}^m(q)$ and $\tilde{d}_{\mu',\mu}^m(q)$ are defined in Eqs. (A5) and (A4).

For the velocity gauge, $\hat{X}=\partial/\partial y$ and $\hat{X}=\partial/\partial z$ for the y and z components of the dipole, respectively. Using expressions of $\partial/\partial y$ and $\partial/\partial z$ in spheroidal coordinates [27] leads to

$$(D_y^V)_\rho^{\rho'} = \frac{(\delta_{m',m+1} - \delta_{m',m-1})}{2i}\frac{R^2}{2^2}\{y_{\nu',\nu}^{m',m}\tilde{t}_{\mu',\mu}^{m',m}(0) - t_{\nu',\nu}^{m',m}(0)\tilde{y}_{\mu',\mu}^{m',m}\} - \frac{m(\delta_{m',m+1} + \delta_{m',m-1})}{2i}\frac{R^2}{2^2} \times\{t_{\nu',\nu}^{m',m}(0)\tilde{x}_{\mu',\mu}^{m',m} + x_{\nu',\nu}^{m',m}\tilde{t}_{\mu',\mu}^{m',m}(0)\}, \quad \text{(B5)}$$

$$(D_z^V)_\rho^{\rho'} = \delta_{m',m}\frac{R^2}{2^2}\{z_{\nu',\nu}^{m}\tilde{d}_{\mu',\mu}^{m}(1) + d_{\nu',\nu}^{m}(1)\tilde{z}_{\mu',\mu}^{m}\}, \quad \text{(B6)}$$

where

$$y_{\nu',\nu}^{m',m} = \int_1^\infty U_{\nu'}^{m'}(\xi)\left(\xi\sqrt{\xi^2-1}\frac{\partial}{\partial\xi}\right)U_\nu^m(\xi)d\xi, \quad \text{(B7)}$$

$$\tilde{y}_{\mu',\mu}^{m',m} = \int_{-1}^{+1} V_{\mu'}^{m'}(\eta)\left(\eta\sqrt{1-\eta^2}\frac{\partial}{\partial\eta}\right)V_\mu^m(\eta)d\eta, \quad \text{(B8)}$$

$$x_{\nu',\nu}^{m',m} = \int_1^\infty U_{\nu'}^{m'}(\xi)U_\nu^m(\xi)\frac{d\xi}{\sqrt{\xi^2-1}}, \quad \text{(B9)}$$

$$\tilde{x}_{\mu',\mu}^{m',m} = \int_{-1}^{+1} V_{\mu'}^{m'}(\eta)V_\nu^m(\eta)\frac{d\eta}{\sqrt{1-\eta^2}}, \quad \text{(B10)}$$

$$z_{\nu',\nu}^{m} = \int_1^\infty U_{\nu'}^{m}(\xi)\left((\xi^2-1)\frac{\partial}{\partial\xi}\right)U_\nu^m(\xi)d\xi, \quad \text{(B11)}$$

$$\tilde{z}_{\mu',\mu}^{m} = \int_{-1}^{+1} V_{\mu'}^{m}(\eta)\left((\eta^2-1)\frac{\partial}{\partial\eta}\right)V_\mu^m(\eta)d\eta. \quad \text{(B12)}$$

In order to evaluate the integrals (B3), (B7), (B9), and (B11), we express their integrands as a sum of products of $e^{-\alpha(\xi-1)}$, polynomials of ξ, and Laguerre polynomials by using Eqs. (7) and (A10), then use the quadrature formula (A9) to evaluate the resulting integral numerically. Here, the quadrature formula is also exact, for the same reasons as mentioned above for the integral (A8).

For the evaluation of $\tilde{t}_{\mu',\mu}^{m+1,m}(q)$, we first use Eq. 8.733.4 of Ref. [28] to show that $V_{\mu'}^{m+1}\eta^q\sqrt{1-\eta^2}V_\mu^m(\eta) = a_1(\mu,m)V_{\mu'}^{m+1}\eta^q V_{\mu-1}^{m+1}(\eta) + a_2(\mu,m)V_{\mu'}^{m+1}\eta^q V_{\mu+1}^{m+1}(\eta)$, where the $a_1(\mu,m)$ and $a_2(\mu,m)$ are functions of μ and m only. Then, applying the recurrence (A11) iteratively for the integer q considered, we further express $V_{\mu'}^{m+1}\eta^q\sqrt{1-\eta^2}V_\mu^m(\eta)$ as a linear combination of $V_{\mu'}^{m+1}V_{\mu\pm p}^{m+1}(\eta)$ (where p is an integer), so that Eq. (A12) could be used. This leads to closed-form analytical expressions for $\tilde{t}_{\mu',\mu}^{m+1,m}$ that we do not reproduce here because they are lengthy. A similar approach using Eq. 8.735.5 of Ref. [28] also yields analytical expressions for $\tilde{t}_{\mu',\mu}^{m-1,m}$.

We could not obtain analytical expressions for the integrals (B8) and (B10). Instead, these integrals are evaluated numerically using the Gauss-Legendre quadrature [40], after expressing $\partial/\partial\eta V_\mu^m(\eta)$ in terms of $V_{\mu\pm1}^m(\eta)$ by means of Eq. 8.733.1 of Ref. [28]. The latter equation also leads to

$$\tilde{z}_{\mu',\mu}^{m} = -\mu\sqrt{\frac{(\mu-m+1)(\mu+m+1)}{(2\mu+1)(2\mu+3)}}\delta_{\mu',\mu+1} + (\mu+1)\sqrt{\frac{(\mu-m)(\mu+m)}{(2\mu-1)(2\mu+1)}}\delta_{\mu',\mu-1}. \quad \text{(B13)}$$

[1] T. Brabec and F. Krausz, Rev. Mod. Phys. **72**, 545 (2000).
[2] M. Drescher *et al.*, Nature (London) **291**, 1923 (2001).
[3] A. D. Bandrauk and N. H. Shon, Phys. Rev. A **66**, 031401(R) (2002).
[4] A. D. Bandrauk and H. Kono, in *Advances in Multi-Photon Processes and Spectroscopy*, edited by S. H. Lin (World Scientific, Singapore, 2003), Vol. 15, p. 147.
[5] S. Chelkowski, C. Foisy, and A. D. Bandrauk, Phys. Rev. A **57**, 1176 (1998).
[6] H. Yu and A. D. Bandrauk, J. Chem. Phys. **102**, 1257 (1995).
[7] A. D. Bandrauk, S. Chelkowski, H. Yu, and E. Constant, Phys. Rev. A **56**, R2537 (1997).
[8] P. B. Corkum, Phys. Rev. Lett. **71**, 1994 (1993).
[9] K. C. Kulander, K. J. Schafer, and J. L. Krause, in *Super Intense Laser Atom Physics*, edited by B. Piraux (Plenum Press, New York, 1993), Vol. 316, p. 95.
[10] H. Nikura *et al.*, Nature (London) **417**, 917 (2002).
[11] F. Légaré, I. V. Litvinynk, P. W. Dooley, F. Quere, A. D.

Bandrauk, D. M. Villeneuve, and P. B. Corkum, Phys. Rev. Lett. **91**, 093002 (2003).
[12] T. Zuo, A. D. Bandrauk, and P. B. Corkum, Chem. Phys. Lett. **259**, 313 (1996).
[13] A. D. Bandrauk, S. Chelkowski, and I. Kawata, Phys. Rev. A **67**, 013407 (2003).
[14] R. Velotta, N. Hay, M. B. Mason, M. Castillejo, and J. P. Marangos, Phys. Rev. Lett. **87**, 183901 (2001).
[15] H. Stapelfeldt and J. Seideman, Rev. Mod. Phys. **75**, 543 (2003).
[16] J. Levesque *et al.* (unpublished).
[17] M. Lein, N. Hay, R. Velotta, J. P. Marangos, and P. L. Knight, Phys. Rev. Lett. **88**, 183903 (2002); Phys. Rev. A **66**, 023805 (2002).
[18] M. Lein, J. P. Marangos, and P. L. Knight, Phys. Rev. A **66**, 051404(R) (2002).
[19] G. Lagmago Kamta and A. D. Bandrauk, Phys. Rev. A **70**, 011404(R) (2004).
[20] P. Antoine, B. Piraux, and A. Maquet, Phys. Rev. A **51**, R1750 (1995), and references therein.
[21] L. V. Vela-Arevalo and J. E. Marsden, Class. Quantum Grav. **21**, S351 (2004).
[22] A. D. Bandrauk and G. Turcotte, J. Chem. Phys. **77**, 3867 (1982).
[23] V. Veniard, R. Taieb, and A. Maquet, Phys. Rev. A **54**, 721 (1996).
[24] K. Burnett, V. C. Reed, J. Cooper, and P. L. Knight, Phys. Rev. A **45**, 3347 (1992).
[25] J. Itatani *et al.*, Nature (London) **432**, 867 (2004).
[26] E. Teller and H. L. Sahlin, in *Physical Chemistry: An Advanced Treatise* (Academic, New York, 1970), Vol. V, p. 35.
[27] M. G. Baik, M. Pont, and R. Shakeshaft, Phys. Rev. A **54**, 1570 (1996).
[28] I. S. Gradshteyn and I. M. Ryzhik, *Table of Integrals, Series and Products*, 5th ed. (Academic Press, New York, 1994).
[29] See, e.g., J. M. Taylor, Z. C. Yan, A. Dalgarno, and J. F. Babb, Mol. Phys. **97**, 23 (1999), and references therein.
[30] S. Barmaki, S. Laulan, H. Bachau, and M. Ghalim, J. Phys. B **36**, 817 (2003); S. Barmaki, H. Bachau, and M. Ghalim, Phys. Rev. A **69**, 043403 (2004).
[31] E. Huens, B. Piraux, A. Bugacov, and M. Gajda, Phys. Rev. A **55**, 2132 (1997).
[32] B. Piraux and R. Shakeshaft, Phys. Rev. A **49**, 3903 (1994).
[33] C. W. McCurdy and C. K. Stroud, Comput. Phys. Commun. **63**, 323 (1991); S. D. Parker and C. W. McCurdy, Chem. Phys. Lett. **156**, 483 (1989).
[34] J. D. Morgan and B. Simon, J. Phys. B **14**, L167 (1981); W. P. Reinhardt, Annu. Rev. Phys. Chem. **33**, 223 (1982); B. R. Junker, Adv. At. Mol. Phys. **18**, 207 (1982); Y. K. Ho, Phys. Rep. **99**, 1 (1983).
[35] P. Froelich, K. Szalewicz, B. Jeziorski, W. Kolos, and H. J. Monkhorst, J. Phys. B **20**, 6173 (1987).
[36] G. Lagmago Kamta, B. Piraux, and A. Scrinzi, Phys. Rev. A **63**, 040502(R) (2001).
[37] R. S. Mulliken, J. Chem. Phys. **7**, 20 (1939).
[38] G. Lagmago Kamta and A. F. Starace, Phys. Rev. A **65**, 053418 (2002).
[39] B. Piraux and G. Lagmago Kamta, in *Super Intense Laser-Atom Physics*, edited by B. Piraux and K. Rzazewski, NATO Science Series II (Kluwer Academic Publishers, Dordrecht, 2001), Vol. 12, p. 127.
[40] W. H. Press, S. A. Teukolski, W. T. Vetterling, and B. P. Flannery, *Numerical Recipes in Fortran: The Art of Scientific Computing*, 2nd Edition (Cambridge, U.P., Cambridge, 1992).
[41] E. Hairer, S. P. Nørsett, and G. Wanner, *Solving Ordinary Differential Equations I: Nonstiff Problems* (Springer-Verlag, Berlin, 1987).
[42] E. Cormier and P. Lambropoulos, J. Phys. B **29**, 1667 (1996).
[43] C. Leubner and P. Zoller, J. Phys. B **13**, 3613 (1980); W. E. Lamb, R. R. Schlicher, and M. O. Scully, Phys. Rev. A **36**, 2763 (1987).
[44] T. Zuo, S. Chelkowski, and A. D. Bandrauk, Phys. Rev. A **49**, 3943 (1994).
[45] S. Kazamias and P. Balcou, Phys. Rev. A **69**, 063416 (2004).
[46] M. Lewenstein, P. Balcou, M. Yu. Ivanov, A. L'Huillier, and P. B. Corkum, Phys. Rev. A **49**, 2117 (1994).
[47] A. D. Bandrauk, S. Chelkowski, and S. Goudreau, J. Mod. Opt. (to be published).
[48] C. A. Coulson, Trans. Faraday Soc. **33**, 1479 (1937).
[49] H. D. Cohen and U. Fano, Phys. Rev. **150**, 30 (1966).
[50] P. Agostini and L. F. DiMauro, Rep. Prog. Phys. **67**, 813 (2004).
[51] G. Yudin, S. Chelkowski, and A. D. Bandrauk (unpublished).
[52] M. Abramowitz and I. A. Stegun, *Handbook of Mathematical Functions with Formulas, Graphs, and Mathematical Tables* (Dover Publications, New York, 1972).